(12)

AD-A164 630

20000801232

CRACK PROPAGATION AND BRANCHING IN BURNING SOLID PROPELLANTS AND IGNITION OF NITRAMINE-BASED COMPOSITE PROPELLANTS

ANNUAL REPORT

Sponsored by
Office of Naval Research
Power Program
Arlington, Virginia
Contract No. N00014-79-C-0762

Prepared by
K. K. Kuo, J. A. Moreci, J. U. Kim, T. Torikai,
M. Grubelich, L. K. Chang, and P. Beelitz

January 1986

THE PENNSYLVANIA STATE UNIVERSITY
College of Engineering
Department of Mechanical Engineering
University Park, Pennsylvania

SECURITY CLASSIFICATION OF THIS PAGE (When Data Entered)

REPORT DOCUMENTATION PAGE

READ INSTRUCTIONS BEFORE COMPLETING FORM

1. REPORT NUMBER	2. GOVT ACCESSION NO. AD-A164 630
	3. RECIPIENT'S CATALOG NUMBER
4. TITLE (and Subtitle) CRACK PROPAGATION AND BRANCHING IN BURNING SOLID PROPELLANTS AND IGNITION OF NITRAMINE-BASED COMPOSITE PROPELLANTS	5. TYPE OF REPORT & PERIOD COVERED Nov. 1,1984 - Dec. 31 1985
	6. PERFORMING ORG. REPORT NUMBER
7. AUTHOR(s) K.K.Kuo, J.A.Moreci,J.U.Kim,T.Torikai, M.Grubelich,L.K.Chang, and P.Beelitz	8. CONTRACT OR GRANT NUMBER(s) N00014-79-C-0762
9. PERFORMING ORGANIZATION NAME AND ADDRESS Department of Mechanical Engineering The Pennsylvania State University University Park, PA 16802	10. PROGRAM ELEMENT, PROJECT, TASK AREA & WORK UNIT NUMBERS
11. CONTROLLING OFFICE NAME AND ADDRESS Office of Naval Research Power Program Arlington, VA 22217	12. REPORT DATE January 1986
	13. NUMBER OF PAGES 114
14. MONITORING AGENCY NAME & ADDRESS(if different from Controlling Office)	15. SECURITY CLASS. (of this report) Unclassified
	15a. DECLASSIFICATION/DOWNGRADING SCHEDULE

16. DISTRIBUTION STATEMENT (of this Report)

Approved for public release; distribution unlimited

17. DISTRIBUTION STATEMENT (of the abstract entered in Block 20, if different from Report)

18. SUPPLEMENTARY NOTES

19. KEY WORDS (Continue on reverse side if necessary and identify by block number)

Ignition, Nitramine propellants, Thermal decomposition, Reaction mechanisms, Ignition delay, Ignition mechanism, CO_2 laser, Crack propagation, Crack branching, Interrupted burning, Depressurization Extinguishment

20. ABSTRACT (Continue on reverse side if necessary and identify by block number)

(See reverse side)

DD FORM 1 JAN 73 1473

Unclassified -- January 31, 1986

SECURITY CLASSIFICATION OF THIS PAGE (When Data Entered)

SECURITY CLASSIFICATION OF THIS PAGE(When Data Entered)

20.

ABSTRACT

Three major tasks performed during the report period of investigation were: (i) crack propagation and branching in burning solid propellants, (ii) ignition of nitramine-based composite propellants under rapid pressurization, and (iii) ignition of nitramine-based composite propellants by CO_2 laser.

Propellant samples have been recovered by interrupted burning experiments. Four modes of crack propagation and/or branching were observed. For very low $\partial p/\partial t$, burning occurs without crack propagation. For $\partial p/\partial t$ in the order of 1.4 to 15 GPa/s, an existing crack propagates along its initial direction as a single crack (propagation mode). At high pressurization rates of 30 GPa/s or higher, multiple branching in various directions is observed exclusively (branched mode), and at intermediate $\partial p/\partial t$, single crack propagation is accompanied by local branching (mixed mode). The amount of surface area generated by mixed or branched modes is substantially higher than that of the single crack propagation mode, and thus could cause sufficiently severe burning in the damaged zone to result in rocket motor failure.

The crack propagation problem is analyzed through the use of basic physical principles, experimental results, and Schapery's theory of crack propagation. A set of governing dimensionless parameters which control and characterize the degree of damage has been obtained. These parameters can be used to develop guidelines for safe operating conditions of rocket motors.

Ignition characteristics of a series of RDX-based composite propellants were studied. The times for the onset of light emission of different propellants under rapid pressurization were compared. The pressurization rates used in the study are typical of ignition transient in rocket motors, so that the results obtained are useful for propulsion system design as well as for selection of appropriate propellant ingredients to achieve desired ignition characteristics. It is found that the time for onset of light emission (t_{LE}) decreases as pressurization rate increases, and t_{LE} depends strongly on propellant ingredients and their mass fractions. It is also found that propellant samples with shorter t_{LE} do not necessarily show higher mass consumption, this indicates that propellant vulnerability should be evaluated by both t_{LE} and the fraction of mass consumed.

CRACK PROPAGATION AND BRANCHING IN BURNING SOLID PROPELLANTS AND IGNITION OF NITRAMINE-BASED COMPOSITE PROPELLANTS

ANNUAL REPORT

Sponsored by

Office of Naval Research
Power Program
Arlignton, Virginia

Contract No. N00014-79-C-0762

Prepared by

Kenneth K. Kuo
John A. Moreci
Jong U. Kim
Takaaki Torikai
Mark Grubelich
Louis K. Chang
Paul Beelitz

Department of Mechanical Engineering
The Pennsylvania State University
University Park, PA 16802

ACKNOWLEDGEMENT

This research has been sponsored by the Power Program of the Office of Naval Research, Arlington, Virginia, under Contract No. N00014-79-C-0762. Dr. Richard S. Miller served as the technical monitor and program manager for this contract. His support of this research investigation is greatly appreciated. We would also like to acknowledge the encouragement of Mr. Tom Boggs of NWC for investigating nitramine propellant ignition. Thanks are due to Drs. Eugene C. Martin and Rena Yee of NWC for providing us with various types of RDX-based composite propellants for our ignition studies. Thanks are also due to Professor Richard A. Schapery of Texas A. & M. University for useful exchange of ideas in crack propagation studies.

TABLE OF CONTENTS

Page

LIST OF FIGURES

Page

Page

LIST OF TABLES

NOMENCLATURE

a	instantaneous crack front location, (L)
a_o	initial crack front location, (L)
A_s	specific surface area generated by damage $= 2(n+1)/(L_d)$, (L^{-1})
b	sample width, (L)
C_{ef}	effective creep compliance, (L^2/F)
E	stored energy of gas phase, (F-L)
h_p	specific enthalpy of propellant product gases, (L^2/t^2)
$h_{t,ign}$	specific total enthalpy of igniter product gases, (L^2/t^2)
K_I	stress intensity factor, $(F/L^{3/2})$
$\dot{K}_I$	dynamic stress intensity factor, $(F/L^{3/2}t)$
L_d	instantaneous crack length $= a - a_o$, (L)
m_{ign}	mass flow rate from igniter, (M/t)
m_{out}	mass flow rate leaving control volume, (M/t)
m_p	mass burning rate of propellant, (M/t)
n	number of statistically averaged macrocracks, (-)

P	pressure, (F/L^2)
Q	rate of heat loss from control volume, $(F\text{-}L/t)$
r_b	propellant burning rate, (L/t)
t	time, (t)
T	temperature, (T)
T_t	stagnation temperature, (T)
V_a	cylindrical volume enclosing the damaged region $= L_d^2 b$, (L^3)
V_c	free chamber volume occupied by the gases in the crack entrance region, (L^3)
V_p	crack propagation velocity $= dL_d/dt$, (L/t)
w	half width of the crack sample, (L)

Greek Symbols

γ	specific heat ratio $(-)$
Γ	fracture energy of the propellant $= (F/L)$
δ	vertical displacement of a propellant strand in the failure zone, (L)

ρ	density, (M/L^3)
ρ_p	propellant density, (M/L^3)
σ	stress distribution in the failure zone, (F/L^2)
Ψ_i	crack entrance half angle, (-)
Ψ_o	sample taper angle, (-)

Subscripts

c	control volume
m	maximum
ss	steady state

I. INTRODUCTION

This annual report summarizes progress made during the period from November 1, 1984 to December 31, 1985, under the project entitled "Ignition of Solid Propellants and Propagation of Burning Propellants Cracks" (Contract No. N00014-79-C-0762).

The overall objective of this investigation is to examine propagation and branching processes in burning solid propellant crack samples and to achieve better understanding of the ignition mechanism of nitramine-based composite propellants. Specific objectives of this study are:

1. to study the mechanism of crack propagation and branching by recovering burning propellant samples;
2. to observe and record crack propagation and branching phenomena in burning solid propellant samples;
3. to determine the effect of pressurization rate and sample geometry on crack propagation velocity;
4. to observe different modes of crack propagation under various pressurization rates;
5. to develop a dimensional analysis in determining a set of governing parameters which control and characterize the degree of damage of solid propellant grain under rapid pressurization;
6. to observe the ignition phenomena of a family of nitramine composite propellants, and to measure ignition delay under various operating conditions;

7. to compare ignition delays of different types of propellant samples under rapid pressurization;

8. to study the effect of bider and oxidizer ingredients on ignition by comparing the ignition processes of propellants with different ingredients;

9. to develop a theoretical model for the ignition of nitramine propellants; and

10. to study the pyrolysis and ignition processes of nitramine-based composite propellants by CO_2 laser.

II. CRACK PROPAGATION AND BRANCHING IN BURNING PROPELLANTS

2.1 Motivation and Objectives

Cracks may exist in solid propellant grains as a result of manufacturing defects, aging, or mechanical damage. In the combustion of these damaged grains, the propagation and branching of cracks may significantly increase the burning surface area in the grain, thus initiating chamber over-pressure and possible rocket motor failure. In seriously damaged grains, these processes could also increase the chance of deflagration-to-detonation transition (DDT). It is the aim of this research to gain deeper understanding of the crack propagation process by experimentally examining modes of damage corresponding to various operating conditions.

The specific objectives of the investigation are:

1) to create damage in propellant samples with prefabricated flaws by rapid pressure loading and combustion;

2) to study the degree of damage produced in the propellant by interrupting the combustion process and recovering the samples before they are consumed;

3) to reveal the major modes of crack propagation and/or branching by characterizing the damage under various pressurization rates; and

4) to determine the key dimensionless parameters governing crack propagation and branching process in burning solid propellants

2.2 Method of Approach

Many variables govern the processes of crack propagation and branching. These include initial pressurization rate, propellant type, sample geometry, initial temperature, etc. The initial pressurization rate is considered to be the most dominant parameter and thus the testing philosophy adopted for this research is to vary the initial pressurization rate while holding other parameters constant. The propellant type under investigation is an AP/HTPB (73/27) composite with an average oxidizer size of 200 μm.

2.2.1 Experimental Setup

In order to generate damage in propellant samples under different initial pressurization rates, and to subsequently recover the samples for examination, a modified version of the experimental setup used in previous studies[1-6] is employed. Major components of the test setup are: 1) a crack propagation test chamber to house the sample and pressure transducers; 2) a driving motor to create high-pressure and high-temperature gases; 3) a depressurization chamber which causes dynamic extinction of

the sample after a desired time interval; 4) a nitrogen injection system which cools the sample and inner surfaces of the test chamber; and 5) a timing control circuit which coordinates the event. A schematic diagram of the test rig and control circuit is shown in Fig. 1.

A two-dimensional sample, with a triangular cavity and an outer taper angle of 3^{o}, is installed in the main chamber and held in position by three brass holders. To seal the propellant in the chamber and provide viewing ports for the event, a plexiglass window and window retainer are bolted into place over the sample. As shown in Fig. 2, there are two window openings in the retainer. The reason for having two view ports instead of one is to avoid window buckling and retainer plate distortion when the chamber is pressurized. The circular port is used to observe combustion product gases as they enter the test chamber from the driving motor. Crack propagation and/or branching can be observed through the rectangular port.

When the main igniter is activated, the propellant sample is pressurized by high-pressure, high-temperature gases. These gases penetrate into the crack cavity causing pressurization, mechanical deformation, crack propagation and/or branching followed by ignition and combustion which produces further damage. The mass and type of charge in the main igniter determines the pressurization rate the sample encounters and, consequently, the mode of damage.

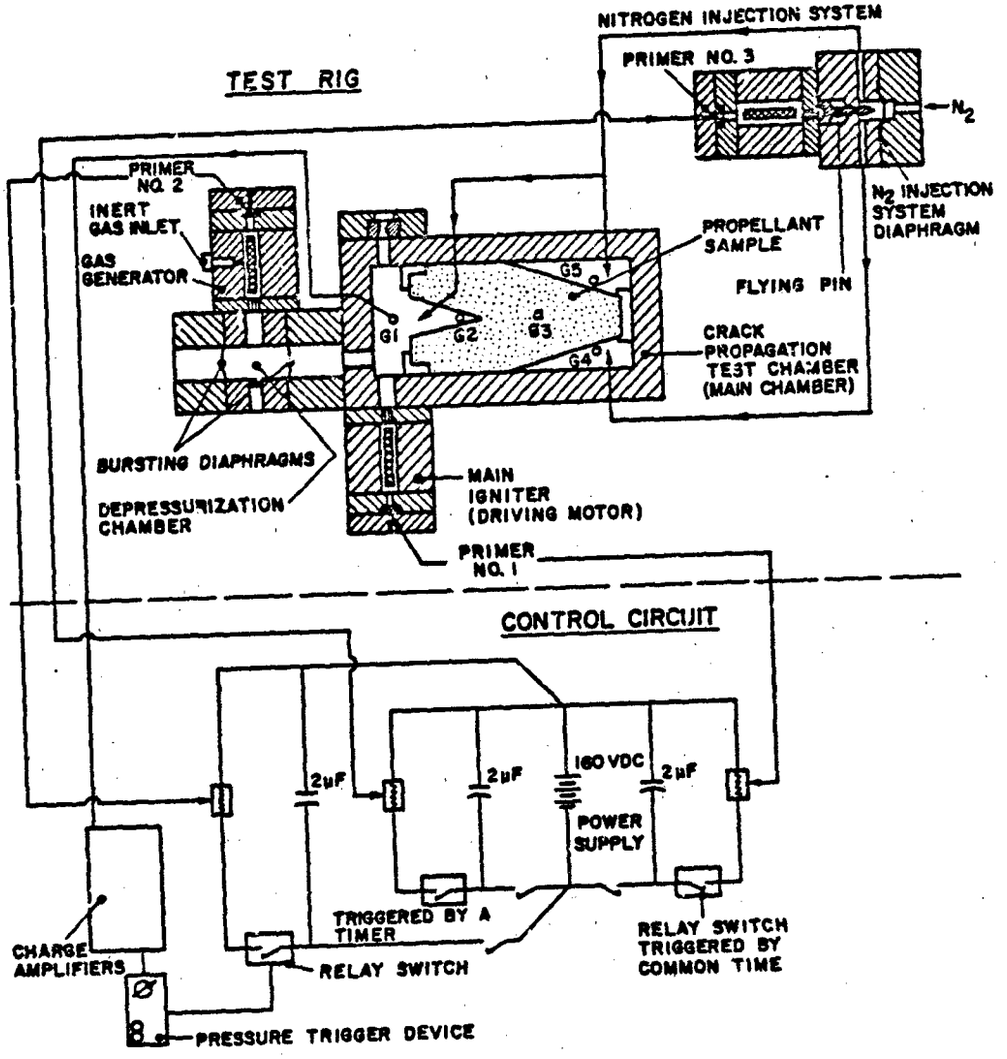

Fig. 1 Schematic Diagram of the Test Rig and Control Circuit for recovery of Propellant Samples During Crack Propagation and/or Branching

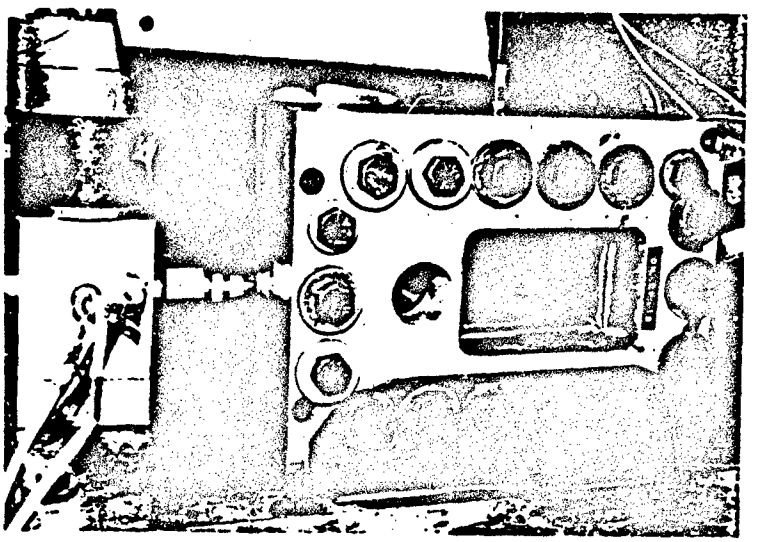

Fig.2 Front View of the Main Chamber and Depressurization Chamber used in Crack Propagation and Branching Studies

To recover the propellant sample the following procedure is used: When the pressure in the main chamber reaches a prescribed value, the timing control circuit activates primer No. 2 located in the depressurization chamber assembly (see Fig. 1). The product gases from the gas generator pressurize the free space between the two bursting diaphragms, causing them to rupture after a short delay. Rapid depressurization of the main chamber follows. The timing control circuit then activates primer No. 3 located in the nitrogen injection system. The product gases from this generator drive the flying pin through the N_2 injection system diaphragm, allowing immediate introduction of low temperature nitrogen into the main chamber for quenching. The time interval between activating primers No. 2 and No. 3 is preselected. The fast change in chamber operating conditions leads the system to dynamic extinction[7], and allows the sample to be recovered.

In some experiments, the depressurization chamber and exit nozzle are replaced by a number of thin brass bursting diaphragms mounted directly on the main chamber. The added area provided by removing the exit nozzle is enough to cause sufficiently rapid depressurization for dynamic extinction. The peak chamber pressure and depressurization rate are controlled in this case by the strength of the bursting diaphragms.

The data acquisition system consists of two major parts: a pressure recording system, and an event filming system. Pressure

measurements are made using 5 piezoelectric transducers mounted on the main chamber against the rear surface of the propellant at the following locations (see Fig. 1): crack cavity entrance (G1), initial crack tip region (G2), center of the sample beyond the initial crack tip (G3), lower cavity (G4), and upper cavity (G5). Pressure signals from the transducers are amplified by charge amplifiers and captured by a transient waveform recorder. A high-speed 16 mm motion picture camera capable of a framing rate of 44,000 pictures per second is used to film the event through the observation ports of the window retainer.

2.3 Experimental Results

Depending upon the initial pressurization rate, four distinct modes of structural damage (Modes A, B, C, and D) at the tip region were observed. The first, Mode A, corresponds to very low $\partial P/\partial t$ (much less than 1 GPa/s) and involves no mechanical damage. The displacement of the crack tip is due solely to recession of the propellant surface by burning. Under this condition, an existing crack will not cause any departure from normal operating conditions. The upper limit of the pressurization rate for this mode depends upon propellant formulation, confinement state, and initial conditions. Since this represents the normal or trivial case of crack propagation, no specific investigation into this area was conducted at this time.

2.3.1 Mode B: Single Crack Propagation

At low pressurization rates, as measured at the entrance of the crack cavity (of the order of 1.4 - 15 GPa/s), single crack propagation was observed. The p-t traces recorded at various locations are shown in Fig. 3. Pressure at the crack entrance increases almost linearly, then decays monotonically after the bursting diaphragms rupture. The maximum pressurization rate at the crack tip (G2) is much higher than that at the G1 location. This indicates that the burning at the crack tip introduces local gas accumulation and damage. However, since the area generated by single crack propagation is limited, it causes no significant pressurization in regions beyond the crack tip, as revealed by the flat p-t traces at locations G3 - G5. The film records of Mode B crack propagation exhibit a triangular crack tip contour during the initial growth period[2]. The crack tip region opens to a rounded crack front contour as a result of severe burning in the damaged zone. After chamber depressurization, the crack front returns to a triangular contour.

Examination of the recovered sample reveals that under these conditions the existing crack is extended in the direction of its initial configuration, as shown in Fig. 4. The characteristic nature of Mode B is such that the damage generated by the loading is restricted to the crack boundary and does not greatly affect the overall integrity of the propellant. The void volume generated is small and does not significantly increase the overall

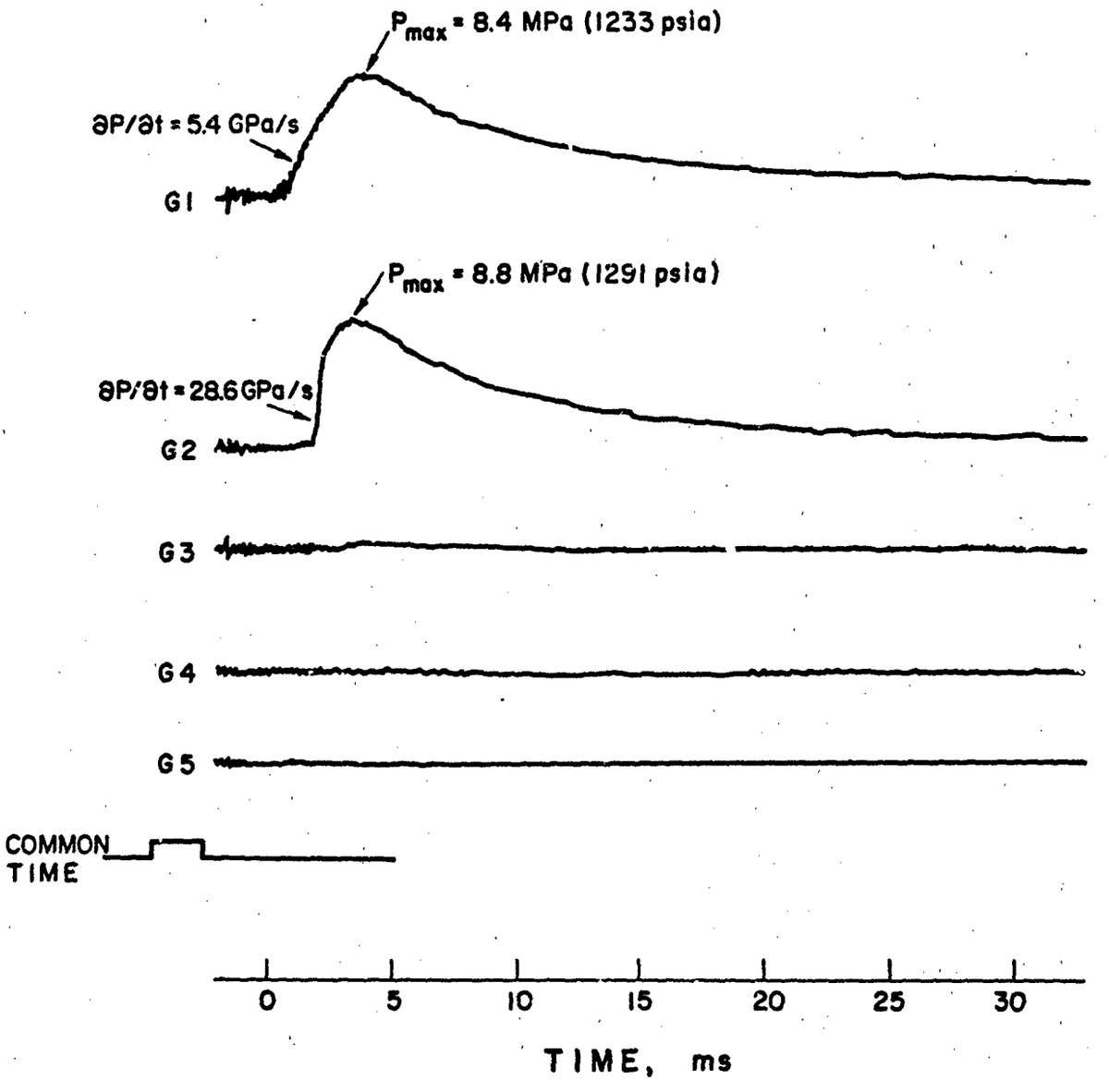

Fig. 3 Pressure-Time Traces of Single Crack Propagation (Test Firing DNICP-24)

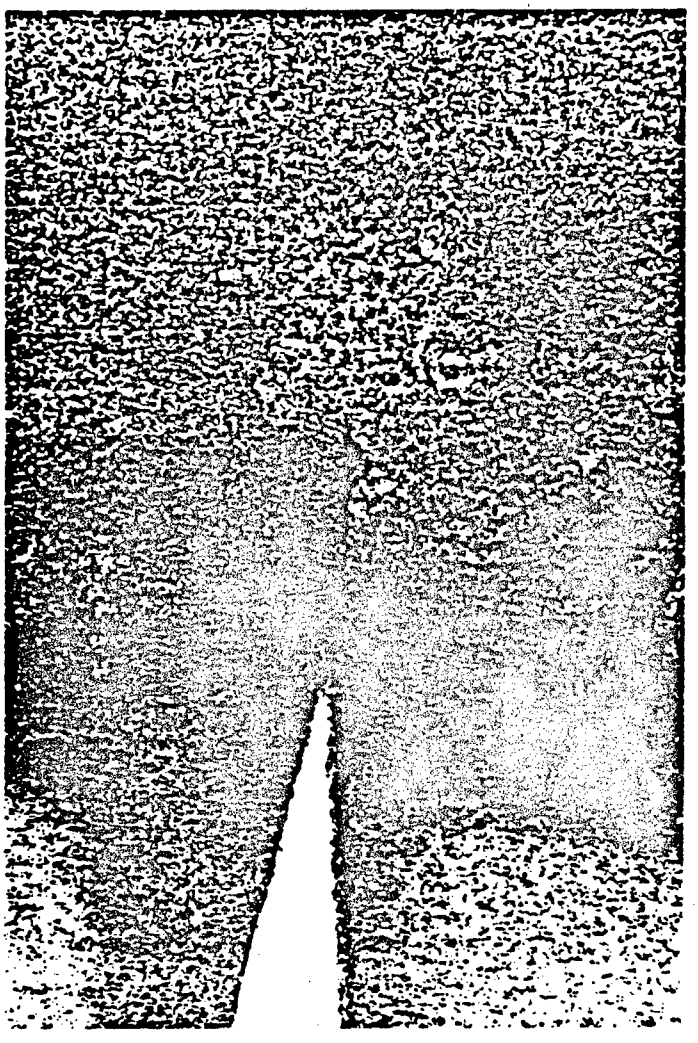

Fig. 4 Recovered Sample exhibiting Mode B Crack Propagation

burning surface area.

2.3.2 Mode C: Crack Propagation with Branching

At intermediate pressurization rates, single crack propagation can be initiated and followed by local branching at various axial locations (see Fig. 5). The damage generated in Mode C is much more extensive than that of Mode B. Figure 6 shows a number of interesting portions of the film event. Detailed interpretation of these film excerpts is presented in Table 1. The recovered propellant sample surface and crack cavity legs are marked by numerous erosion ditches. The surface roughness on the legs before the crack tip is caused by the high-pressure high-temperature gases, which erode the propellant sample as they exit the high pressure zone. The total specific surface area created in Mode C is higher than that of Mode B. Local branching is caused by the excess amount of energy supplied by the driving motor gases above the energy level that a single crack can dissipate.

2.3.3 Mode D: Crack Branching

The crack branching mode involves the development of multiple cracks originating from a central point. Crack branches emanate from this common point and propagate in different directions. This mode can be subdivided into two groups (Mode D_1 and

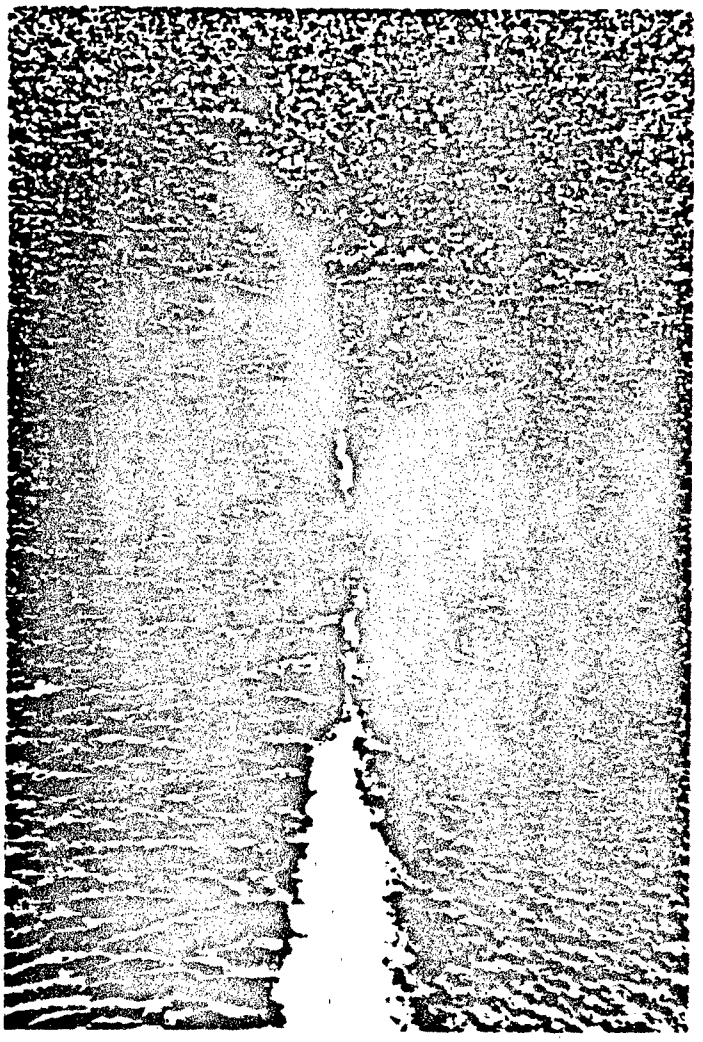

Fig. 5 Recovered Sample exhibiting Mode C Crack Propagation and Branching

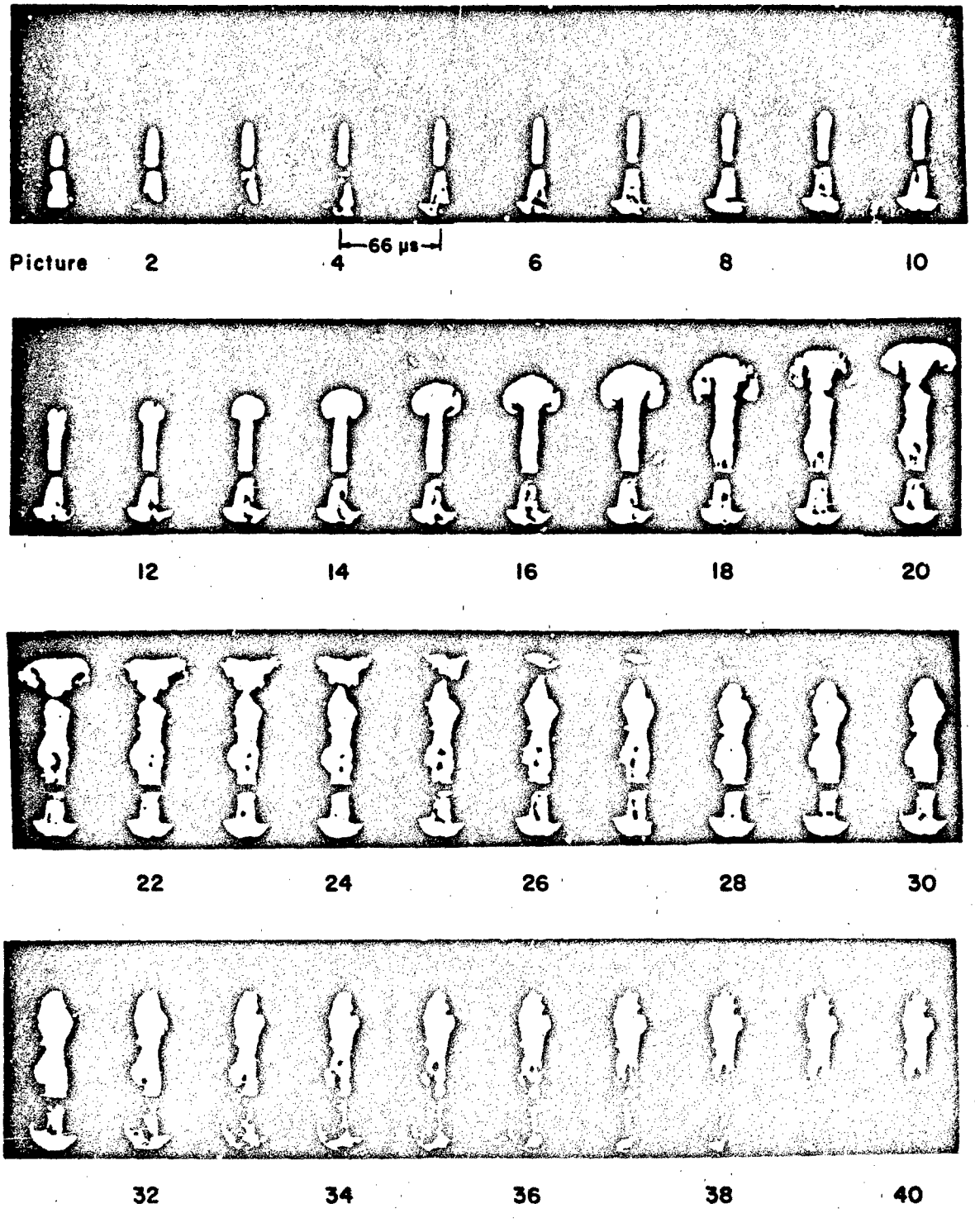

Fig. 6 Film Record of Mode C Crack Propagation and Branching (Test Firing No. DMICP-28)

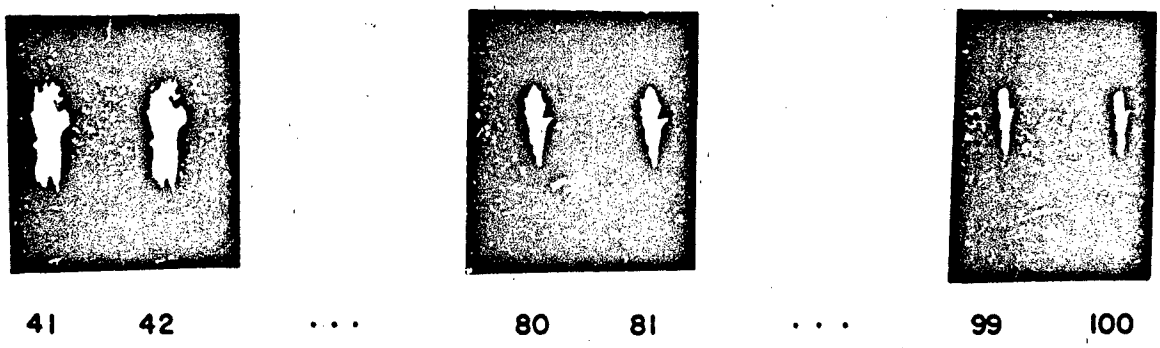

Fig. 6 (con't) Film Record of Mode C Crack Propagation and Branching (Test Firing No. DNICP-28)

Table 1

Film Interpretation of Multiple Crack Propagation and Branching
(Test Firing No. DNICP-28)

(a) Initial Phase of Crack Propagation and Branching

Picture	Time (μs)	Observations and Interpretations
1 - 6	0 - 330	Hot gas penetration into the triangular crack cavity.
7 - 10	396 - 594	Initiation of Crack Growth (propagation).
11	660	Tendency for bifurcation (Initiation of crack branching).
12 - 24	726 - 1,518	Severe burning is evident in damaged region where crack has split into two major branches. The left branch further splits into several smaller subbranches while it continues to propagate. As a result of the enormous amount of local gas generation, high pressure gradients exist between burned and unburned zones. This causes luminous gases to flow beyond the crack front and into the space between sample and window. Penetrating combustion gases in the side cavity are less luminous. Mushroomed region flattens out and becomes less visible on the edge, due to heat loss and, possibly, closing of gap between window and propellant. The left side of sample burns severely and causes more damage to the propellant.

(b) Extinction Phase

Picture	Time (μs)	Observations and Interpretations
25 - 62	1,650 - 4,026	Flame penetrated region between sample and plexiglass window diminishes, thus enhancing visibility of crack tip location.
63 - 100	4,092 - 6,534	The luminous region decreases as depressurization of the chamber continues.

Mode D_2), depending upon the number of major crack branches. Mode D_1 is associated with fewer branches, sometimes only two, where it may be called bifurcation (see Fig. 7). Mode D_2 is associated with numerous branches (see Fig. 8). A typical set of p-t traces representative of Mode D_1 branching is shown in Fig. 9. This test run corresponds to a very high pressurization rate (42 GPa/s) at location G1. The recovered sample shown in Fig. 7 reveals that the crack branches and propagates into two major cracks with several short secondary macrocracks. The high initial gas loading rate generates pressure waves which oscillate within the crack cavity and throughout the propellant sample. As a result of the large increase in specific burning area generated from crack branching at the tip, the pressure history at the center of the sample (G3) is substantially different than the previous case shown in Fig. 3. The p-t trace at G3 shows that the sample in the damaged zone sensed significant pressure loading caused by the partial burning and flame penetration in this region.

Film records of test firings with branched Mode D_1 or D_2 show rapid changes in crack contours, followed by flame penetration between the propellant samples and the sacrificial windows. The flame penetration is caused by steep pressure gradients which exist between the burned and unburned regions. These film records are omitted in this paper; more detailed information is available in Ref. 2. A set of instantaneous crack contours for Mode D_1 is shown in Fig. 10. It is evident that the crack front

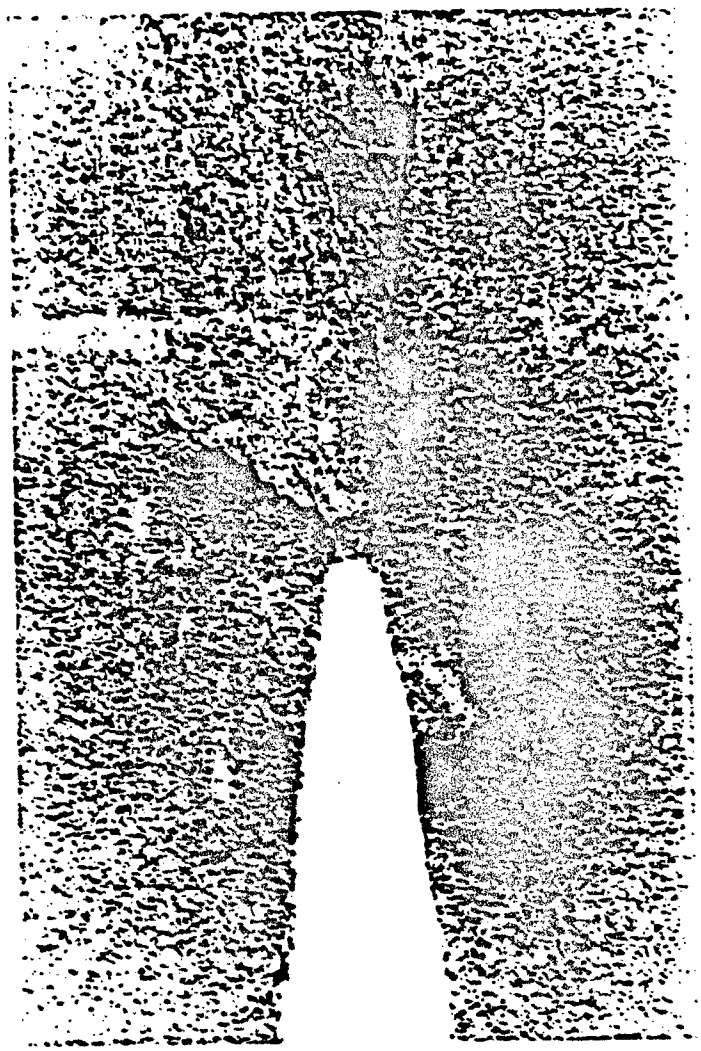

Fig. 7 Recovered Sample exhibiting Mode D_1 Crack Branching

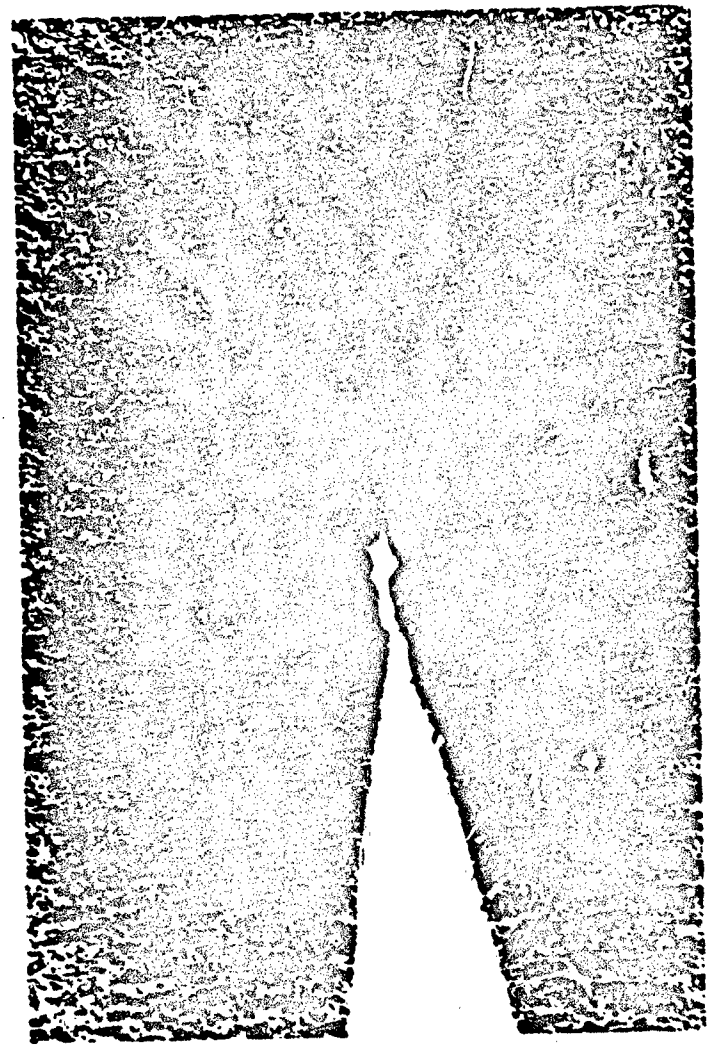

Fig. 8 Recovered Sample exhibiting Mode D_2 Crack Branching

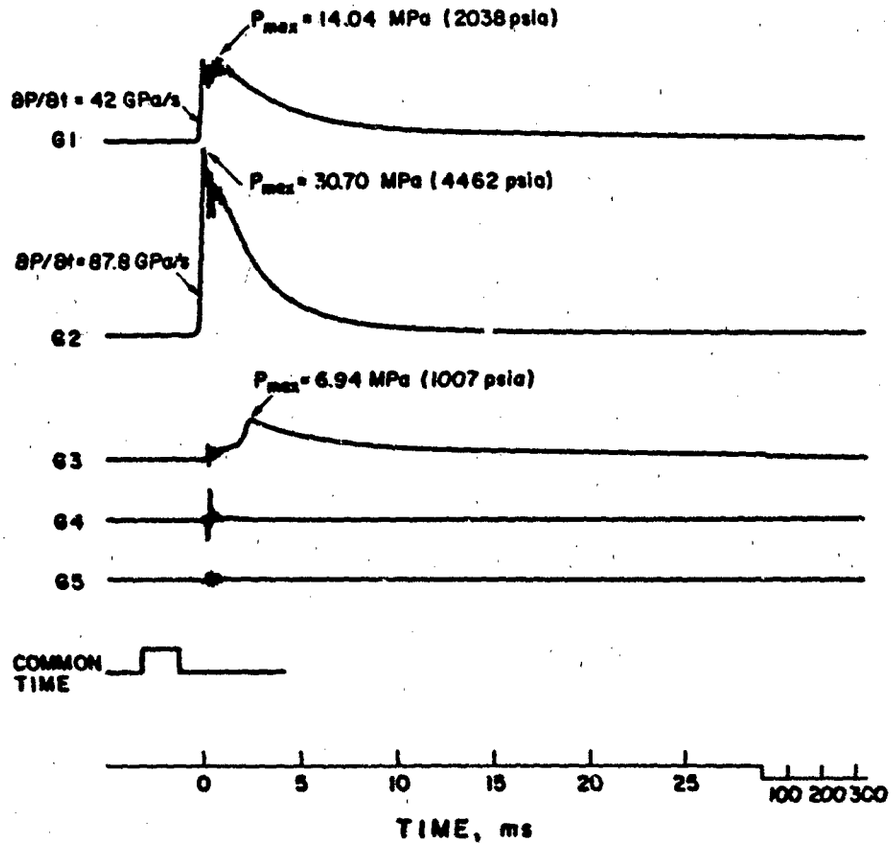

Fig. 9 Pressure-Time Traces of Mode D Crack Branching (Test Firing DNICP-27)

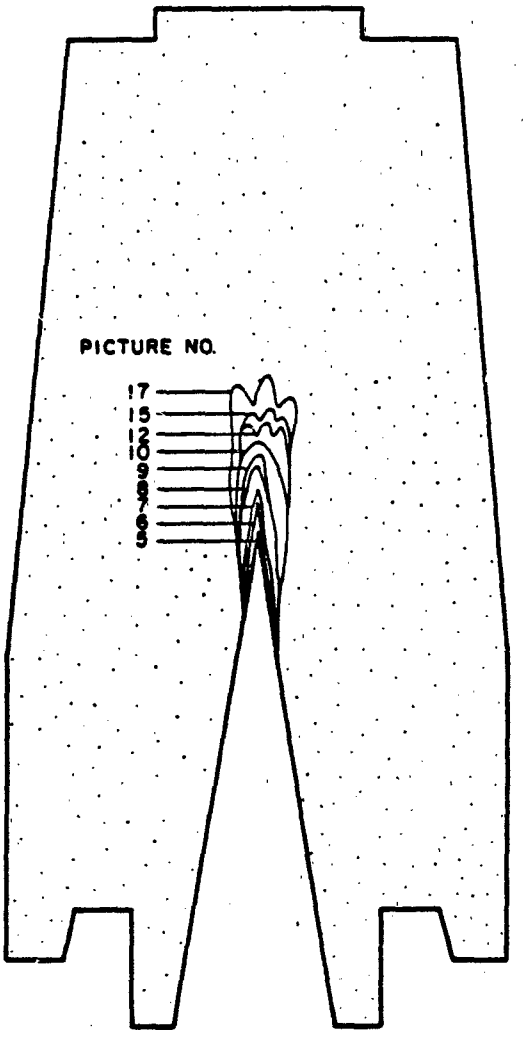

Fig. 10 Instantaneous Mode D_1 Crack Front Contours

transforms from a triangular shape into a round contour and then becomes jagged as branching occurs.

Recovered Mode D_1 and D_2 samples (Figs. 7 and 8) with those of Modes B (Fig. 4) reveals an area of much greater damage near the crack tip compared to single crack propagation. The generation of multiple cracks at very high pressurization rates is mostly a result of the simultaneous attainment of critical stress for fracture at numerous points in the same central area. Following the creation of flow channels, high pressure gases penetrate the local void regions and cause additional damage along the crack branches. This is fundamentally different from the opening mode of single crack propagation which takes place via a relatively slow splitting action.

2.3.4 Comparison of the Crack Propagation Modes

By examining film records, the advancement of crack front location as a function of time is determined and shown in Figs. 11a, 11b, and 11c for Modes B, C, and D respectively. It is not evident that the crack propagation speeds for Modes C and D are higher than for those of Mode B. The reasons are discussed below.

To facilitate analysis of the dependence of crack propagation speed on pressurization rate, the steady state crack front velocities are plotted against the initial pressurization rate as

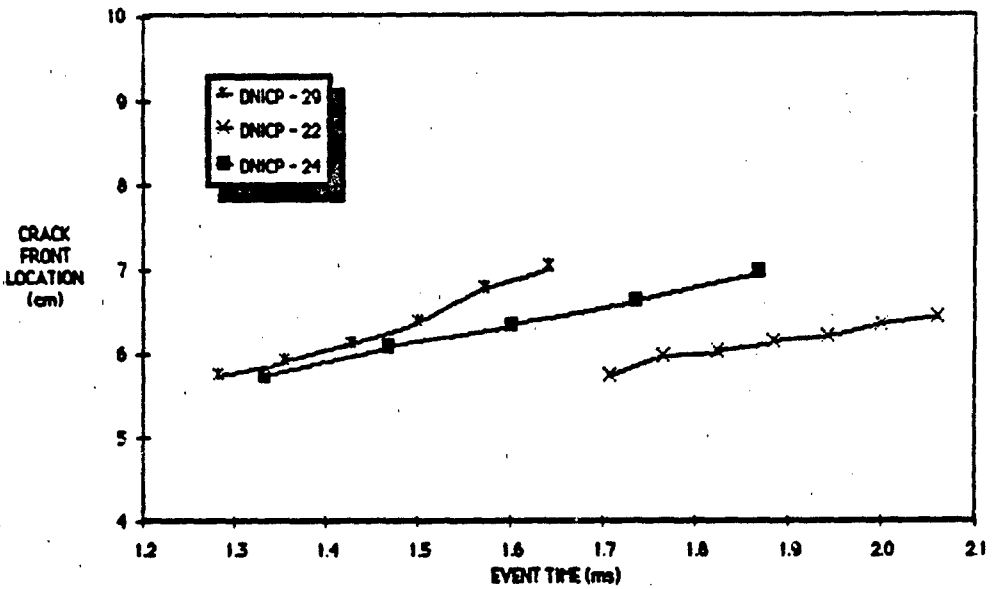

Fig. 11a Crack Front Location as a function of time for Mode B Crack Propagation

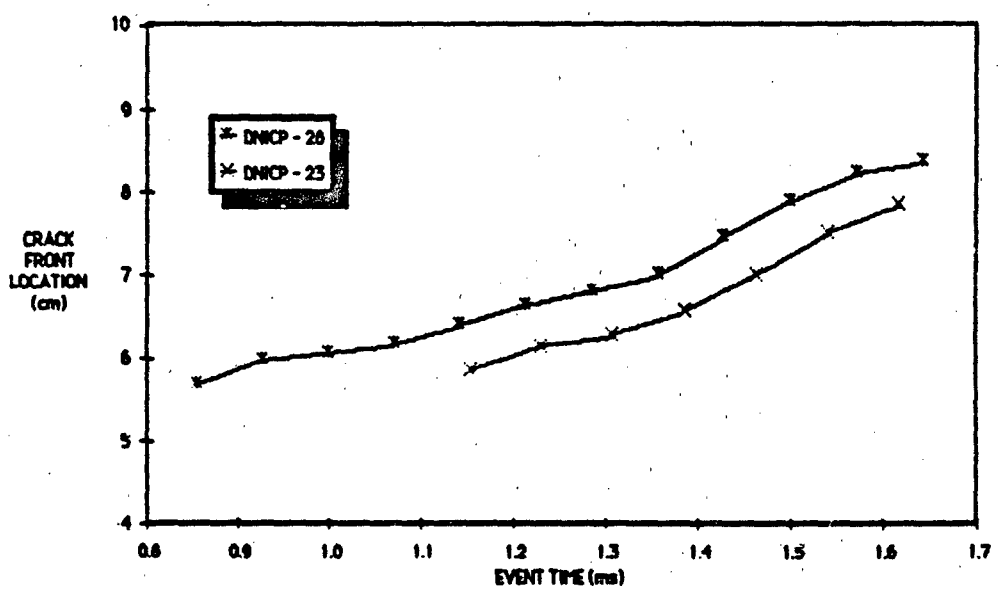

Fig. 11b Crack Front Location as a function of time for Mode C Crack Propagation and Branching

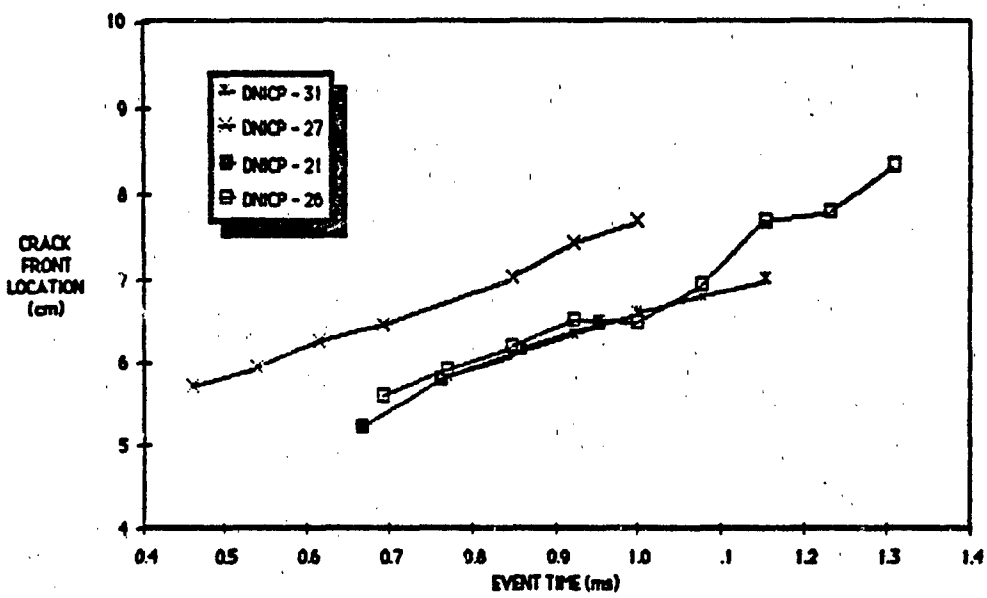

Fig. 11c Crack Front Location as a function of time for Mode D Crack Branching

measured at location G1 for a series of test cases (see Fig. 12). The steady state crack propagation velocity is determined from the best linear fit of the data after the attainment of relatively constant crack front displacement. It is clear that for single crack propagation (Mode B) the steady state crack front velocity, $V_{p,ss}$, increases linearly with $\partial P/\partial t$. At a pressurization rate of approximately 15 GPa/s, the energy input from the driving motor is greater than the maximum dissipation rate for a single propagating crack. Consequently, a transition to a new failure mechanism becomes apparent. In this transition region, either Mode C or D may occur. The factor regulating which mode occurs is believed to be the inhomogeneity of the propellant. The existence or lack of flaws and inclusions within the propellant affect the branching mechanism.

Just beyond the transition point, the crack front velocity reaches its limiting value and begins to decrease. With the existence of multiple cracks, the crack front velocity can be less than that of a single crack; multiple cracks propagating at a slower speed can dissipate higher amounts of energy compared to a single crack propagating at a faster rate. For test firings at initial pressurization rates in excess of 30 GPa/s, the crack branching mechanism dominates.

The shaded region shown on Fig. 12 represents a range of variations of $V_{p,ss}$ with $\partial P/\partial t$. This variation is caused by uncertainties of material properties and geometric factors near

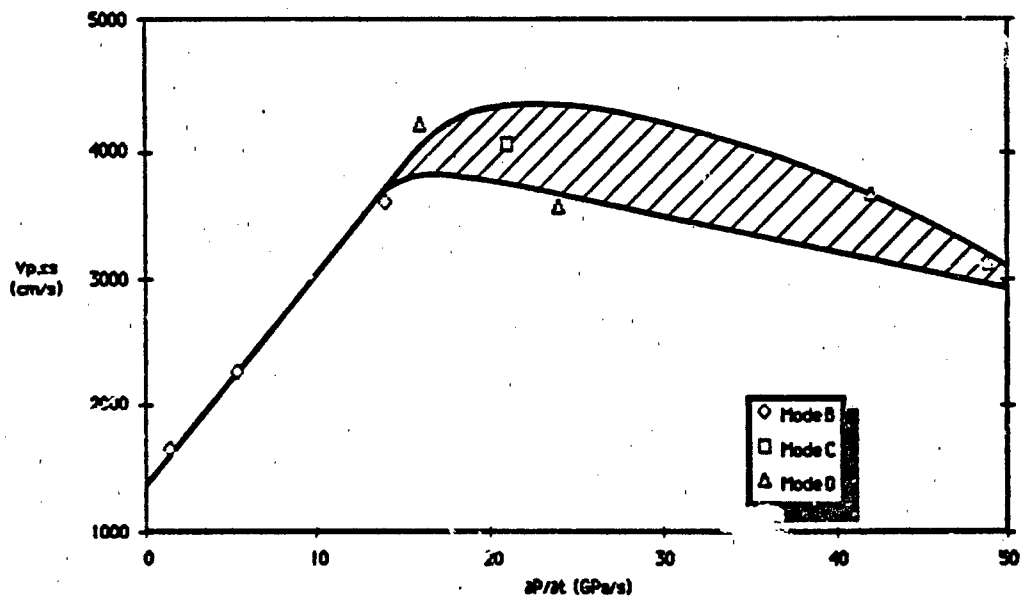

Fig. 12 Steady State Crack Propagation Velocity as a function of Initial Pressurization Rate

the damaged zone. Multiple cracks originate at very high pressurization rates indicating that critical stress for fracture occured simultaneously at many points in the same local area. With the existence of multiple branches, the crack front velocity decreases slightly as the initial pressurization rate increases. However, if the pressurization rate is increased beyond the maximum value tested, $V_{p,ss}$ may start to increase again.

Figure 13 illustrates the time delay for onset of crack propagation and branching as a function of initial pressurization rate. As expected, the time delay associated with single crack propagation is longer than those for Modes C and D. With increasing pressurization rate, and hence energy input rate to the propellant, the delay time decreases for all modes. When the transition point of 15 GPa/s is reached, the delay time varies depending upon the mode of damage. Again the shaded region represents the uncertainty due to material inhomogeneity and geometric factors.

The number of observed macrocracks as a function of initial pressurization rate is given in Fig. 14. As expected for single crack propagation, n is unity up to the transition point. After the transition point, n varies depending upon the mode of damage and uncertainties mentioned above. The number of cracks produced is predominately a function of the energy input rate and the maximum dissipation rate of a single crack. The energy dissipation rate is dependent upon the product of the number of cracks

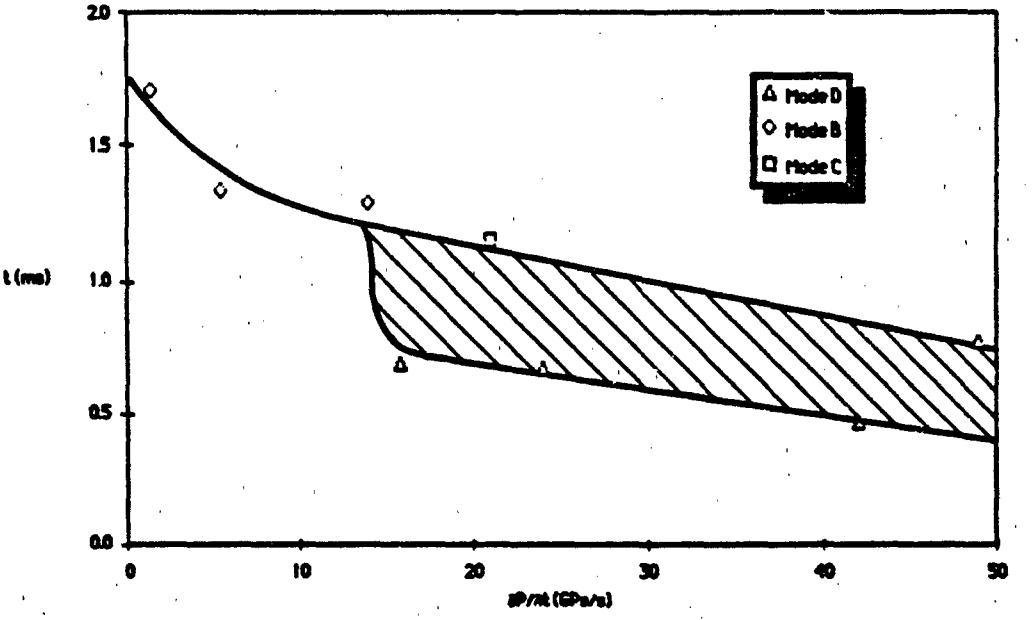

Fig. 13 The Variation of Time Delay for Onset of Crack Propagation and/or Branching as a function of Initial Pressurization Rate

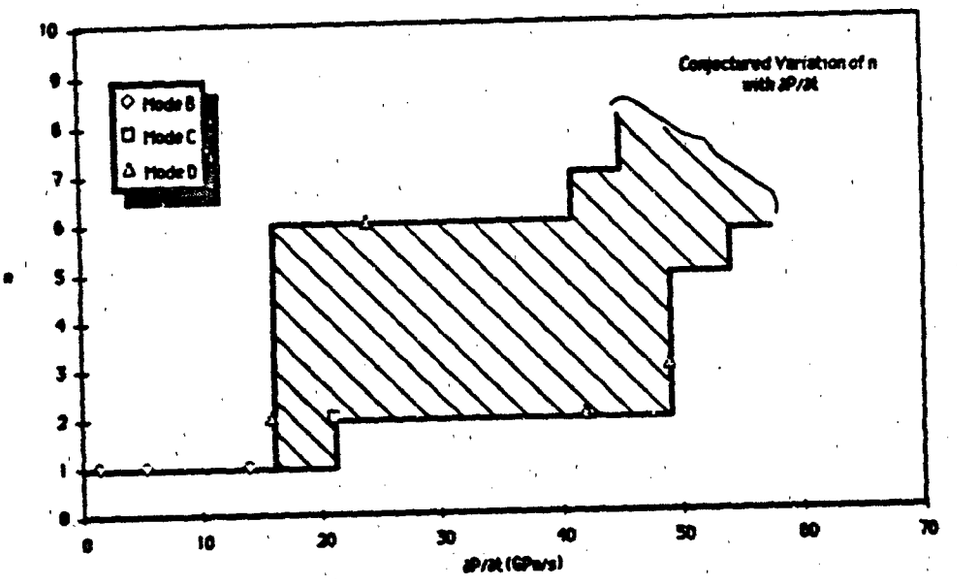

Fig. 14 Number of Observed Cracks as a function of Initial Pressurization Rate

and the crack front velocity. Since for a given energy dissipation rate there are many possible combinations of n and $V_{p,ss}$ there is an envelope of possible values of n after the transition point.

2.4 Analysis

The crack propagation and branching process is inherently a coupled solid mechanics - combustion problem and presents a formidable challenge. However, using a combination of basic physical principles, experimental results, and Schapery's theory of crack propagation[8] (which was developed from an earlier work of Mueller and Knauss[9] and has been verified by comparison with their data), a set of governing dimensionless parameters are deduced through the use of the Buckingham Π Theorem. Five dimensionless parameters and two shape factors are evolved from this approach. Figures 15 and 16 show the damaged sample geometry and the crack tip failure zone considered in the analysis.

2.4.1 Functional Relationships between Physical Parameters

To establish the functional relationships between the physical parameters of the problem, the energy equation applied to the control volume shown in Fig. 17, Schapery's theories on crack propagation in viscoelastic materials, and interpretations

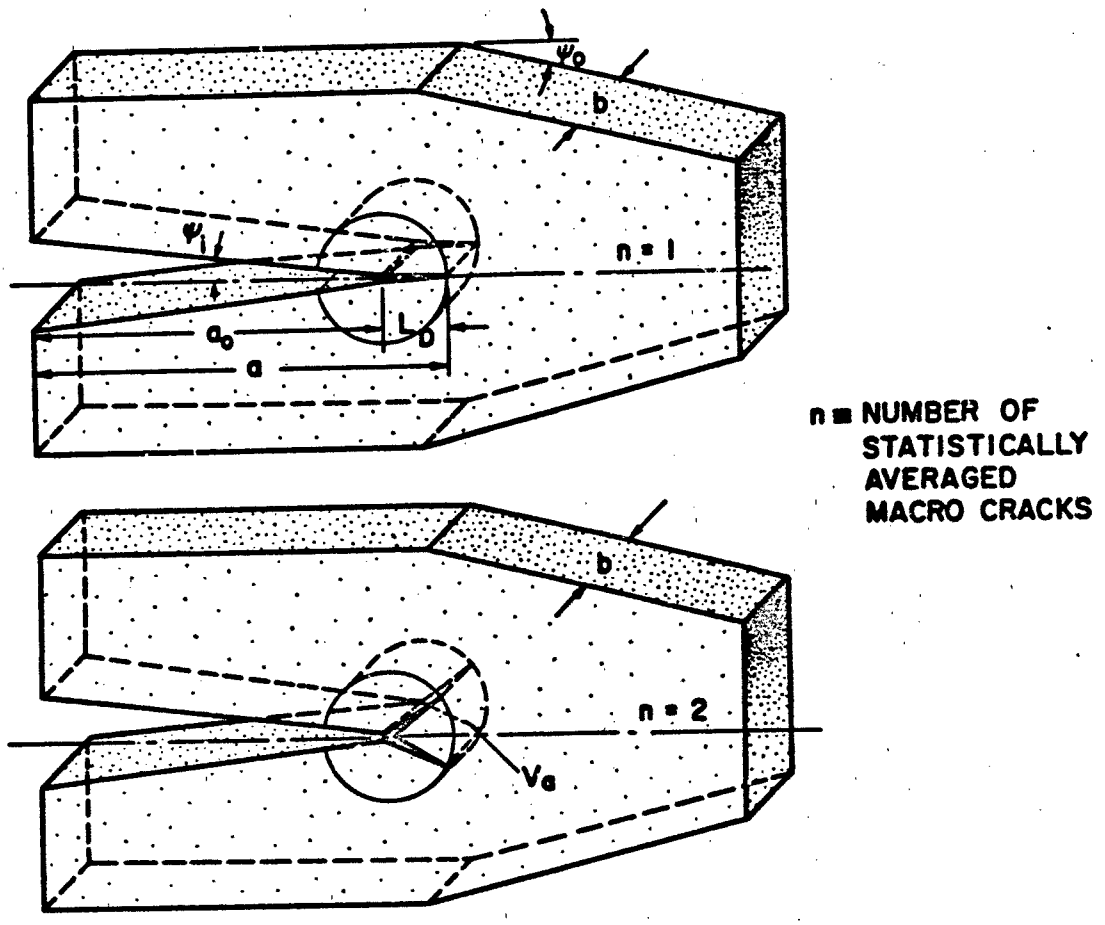

Fig. 15 Damaged Sample Geometry

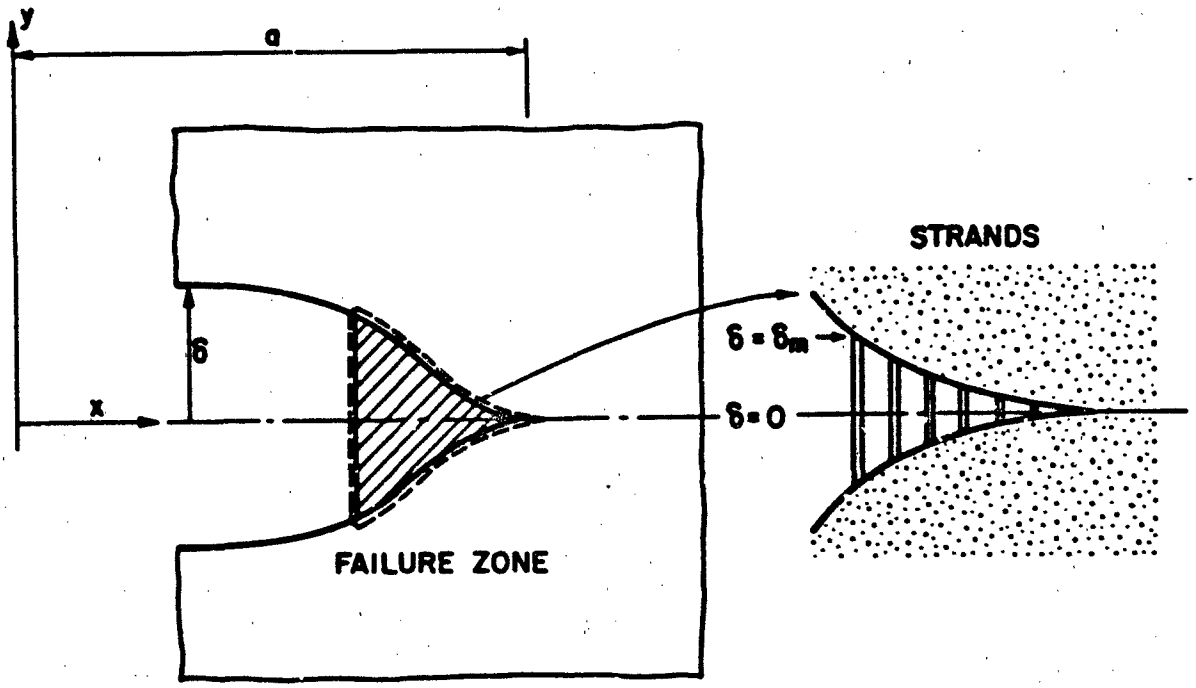

Fig. 16 Schapery's Crack Model

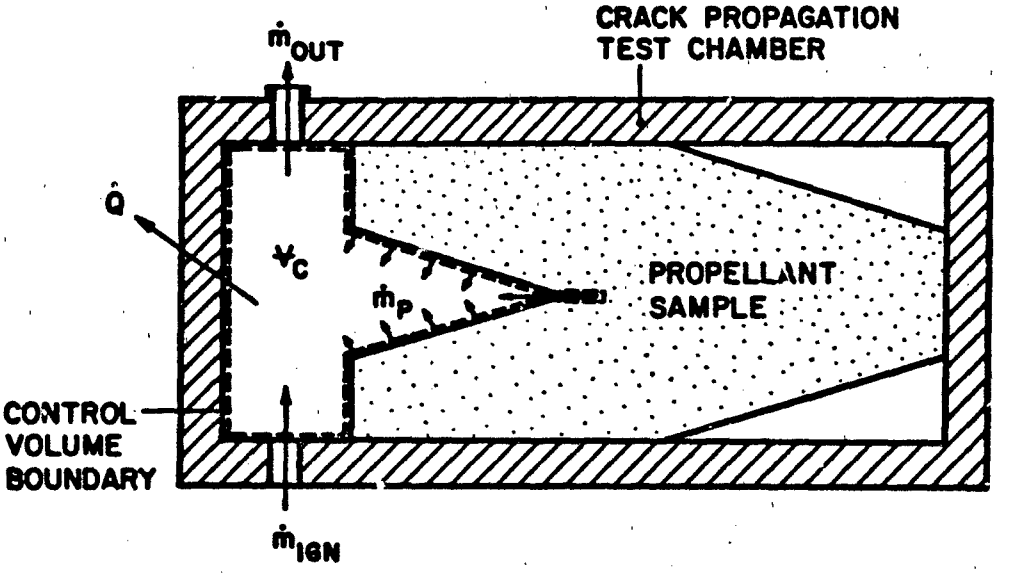

Fig. 17 Control Volume used in Energy Analysis

of results from the crack propagation experiments are used.

The basic assumptions in the analysis are listed below.

1. The heat loss from the control volume to the surroundings is negligible since the damage occurs in an extremely short time interval of the order of 10 ms.

2. The hot combustion gases of the driving motor are considered to follow the perfect gas law. This assumption is valid since the gas temperature is very high (2000 K) and the maximum chamber pressure is less than 35 MPa.

3. Since the initial damage occurs before the bursting diaphragms rupture, $\dot{m}_{out} = 0$ for the time of interest.

4. The gas-phase control volume can be treated as constant since the actual volume increase due to flow work and surface burning is extremely small compared to the total control volume during the time of interest.

The energy equation for the gas phase in the control volume can be written as:

$$\frac{dE}{dt} = \frac{d}{dt}(\rho_c V_c c_v T_c) =$$

$$\dot{m}_{ign} h_{t,ign} + \dot{m}_p h_p - \dot{m}_{out} c_p T \quad - Q - P\frac{\partial V_c}{\partial t} \tag{1}$$

Using the basic assumptions, Eq. (1) reduces to:

$$\frac{V_c}{\gamma - 1}\frac{\partial P}{\partial t} = \dot{m}_{ign} h_{t,ign} + \dot{m}_p h_p \tag{1a}$$

After replacing $\dot{m}_p$ with ρ_p , r_b, and burning surface area, which can further be expressed in terms of geometric parameters, Eq. (1a) has the following functional form:

$$\frac{\partial P_c}{\partial t}\ (V_c, \dot{m}_{ign}, h_{t,ign}, r_b, V_a, a_0, L_d, \rho_p, \psi_i, A_s, h_p) \tag{1b}$$

Following Schapery[8,10] and Mueller and Knauss[9], the relationships between the material properties, damage zone length and the crack propagation velocity are given by:

$$\Gamma = \Gamma(K_I, V_p, \sigma_{fm}) \tag{2}$$

$$L_d = L_d(K_I, \sigma_{fm}) \tag{3}$$

$$V_p = V_p(K_I, \dot{K}_I, \Gamma, C_{ef}, L_d) \tag{4}$$

Since the $\dot{K}_I$ effect is not well defined and measured[10], its inf-

luence on crack propagation is neglected in the present analysis. In the future when data becomes available this effect could be incorporated. Equation (4) then becomes:

$$V_p = V_p(K_I, \Gamma, C_{ef}, L_d) \tag{4a}$$

From evidence obtained in the crack propagation experiments, the crack propagation velocity is related to the following parameters:

$$V_p = V_p(\frac{\partial P}{\partial t}, \Gamma, \psi_i, \psi_o, A_s, V_c, P, m_{ign}) \tag{5}$$

The burning rate of the propellant with a fixed initial temperature depends upon the instantaneous chamber pressure and pressurization rate, i.e.:

$$r_b = r_b(P, \frac{\partial P}{\partial t}) \tag{6}$$

The stress intensity factor for opening mode fracture can be expressed in the following general form[11]:

$$K_I = K_I(a_o, \psi_i, \psi_o, P_c, w) \tag{7}$$

where the half sample width, w, may not be an important parameter since the stress wave propagation in the transverse direction

does not cause the side surfaces of the crack sample to oscillate. Also, experimental observations from the test results show that the inner side surfaces of the crack are flat and spatially fixed. Hence Eq. (7) can be simplified to yield:

$$K_I = K_I(a_o, \psi_i, \psi_o, P_c) \tag{7a}$$

From the geometric relationships, the affected volume (V_a) and specific surface area (A_s) can be written as:

$$V_a = V_a(L_d, b) \tag{8}$$

$$A_s = A_s(n, L_d) \tag{9}$$

The enthalpy of the propellant product gases can be related to the stagnation enthalpy of the igniter gases if the ignition charge is made of the same propellant, i.e.:

$$h_p = \frac{2}{\gamma + 1} h_{t,ign} \tag{10}$$

This equation is arrived at by assuming the flow is choked at the igniter exit port.

The propellant density can be treated as a constant since most propellants are incompressible. Also the variation in den-

sity from one propellant to another is usually very small. Hence:

$$\rho_p = \text{constant} \tag{11}$$

Equations (1b), (2), (3), (4), (5), (6), (7a), (8), (9), (10) and (11) relate the twenty-one parameters affecting the crack propagation process. These eleven equations may be reduced to one equation involving the eleven more significant parameters of the form:

$$V_p = V_p\left(\frac{\partial P}{\partial t}, m_{ign}, V_c, h_{t,ign}, \Gamma, V_a, \psi_i, \psi_o, A_s, L_d\right) \tag{12}$$

It should be noted that the rate of increase of the gas-phase temperature can be related to $\partial P/\partial t$, m_{ign}, and V_c through the use of mass continuity. However, this relationship is not considered important during the initial phase of crack propagation.

2.4.2 Arrangement of the Parameters Governing Crack Propagation into Meaningful Dimensionless Groups

Equation (12) relates the important parameters governing the crack propagation and branching process. By performing a dimen-

sional analysis, these eleven parameters can be resolved into five dimensionless Π's and two shape factors Ψ_i and Ψ_o. Four of the dimensionless Π's characterize the damage produced in the propellant by the energy input from the igniter which is represented by the fifth Π, Π_E. The Π's are defined as follows:

$$\Pi_A \equiv \frac{L_d}{V_c^{1/3}} =$$

$$\frac{\text{Length of Representative Macrocrack}}{\text{Characteristic Length of Free Chamber Volume}} \qquad (13)$$

$$\Pi_B \equiv \frac{2nbV_p}{V_p/A_s} = \frac{4b}{\pi}\left[\frac{(n)(n+1)}{L_d}\right] =$$

$$\frac{\text{Rate of Increase of Crack Surface Area}}{\text{Rate of Increase of Crossectional Area of the Affected Region}} \qquad (14)$$

$$\Pi_C \equiv \frac{V_p}{h_{t,ign}^{1/2}} =$$

$$\frac{\text{Crack Propagation Velocity}}{\text{Speed of Sound in the Igniter Product Gases}} \qquad (15)$$

$$\Pi_D \equiv n =$$

$$\text{Number of Macrocracks with Length, } L_d, \text{ and Depth, } b \qquad (16)$$

$$\Pi_E \equiv \frac{(\frac{\partial P}{\partial t})\pi^3_{ign} h_{t,ign}}{\Gamma^4 V_c^{1/3}} =$$

$$\frac{\text{Energy of Pressurizing Stream per Unit Surface Area}}{\text{Failure Energy of Material in the Damaged Zone}} \qquad (17)$$

Even though the exponent of $\partial P/\partial t$ is unity in Eq. 17, $\partial P/\partial t$ has a very strong influence on crack propagation. It can be seen from Eq. (1)a that $\partial P/\partial t$ is proportional to m_{ign} if the energy input from the propellant sample is negligible. From the functional form of Π_E , it can also be seen that Π_E is highly sensitive to the fracture energy of the propellant.

2.4.3 Anticipated Functional Relationships

Since not all of the material properties of the propellant are yet determined, the values of the dimensionless functional relationships are unknown at the present time. However, from the experimental results and the plots shown in Figs. 12 and 14, the functional relationships can be conjectured.

Since Π_E is strongly affected by the changes of m_{ign} and P/t, the anticipated functional relationships between Π_C and Π_E and Π_D and Π_E are similar to the profiles of $V_{p,ss}$ verses $\partial P/\partial t$ and n verses $\partial P/\partial t$ shown in Figs. 12 and 14 respectively.

It is anticipated that nondimensional effective crack length will increase with energy input parameter Π_E . As expected for the trivial crack propagation case Π_A is nearly equal to zero in the Mode A region. As Mode B single crack propagation occurs, L_d should increase monotonically as the energy input increases. The trends for Modes C and D are not obvious since the number of cracks may increase drastically resulting in shorter average crack length. The value of L_d may therefore increase, decrease or remain constant for these modes.

From Eq. (14), it is seen that Π_B is highly dependent upon n and to a much lesser extent on L_d. By considering the dependence of Π_C and Π_A on Π_E , the dependence of Π_B^* on Π_E is anticipated to be quite strong. For single crack propagation, the value of Π_B is expected to rise to some finite value and then decay slightly as the energy input increases since when only one crack is propagating, the crack surface area does not increase as fast as the cross-sectional area of V_a. When single crack propagation is accompanied by branching (mixed mode), the amount of surface area generated by the cracks grows more rapidly than the cross-sectional area of the affected region. When crack branching occurs the amount of crack surface area generated will far exceed the increase in the cross-sectional area of the affected region.

The anticipated mathematical relationships between the Π's characterizing the degree of damage and the forcing function,

Π_E , are as follows:

$$\Pi_A = \Pi_A(\Pi_E, \psi_i, \psi_o) \tag{18}$$

$$\Pi_B = \Pi_B(\Pi_E, \psi_i, \psi_o) \tag{19}$$

$$\Pi_C = \Pi_C(\Pi_E, \psi_i, \psi_o,) \tag{20}$$

$$\Pi_D = \Pi_D(\Pi_E, \psi_i, \psi_o,) \tag{21}$$

2.5 Summary and Conclusions on Crack Propagation and Branching Studies

Several important observations and conclusions obtained from the crack propagation studies are summarized below:

(1) Propellant samples recovered from test firings exhibited four different modes of damage. Depending upon the initial pressurization rate, the mechanical damage of the sample adjacent to the crack tip region differs significantly. The first mode (Mode A) involves no mechanical damage. Under this condition, an existing crack will not cause any departure from normal motor operating characteristics. The second mode (Mode B) which occurs at relatively low pressurization rates (1.4 - 15 GPa/s), creates local damage restricted to single crack propagation. Such single crack propagation, if continued over a period of time, may cause motor case burn through or other undesirable burning conditions.

(2) The third and fourth modes (Modes C and D) were observed at high pressurization rates. These modes involve crack propagation and multiple branching of the tip region in various directions, generating either small or large amounts of void fractions. These modes can produce high degrees of damage due to the strong interaction between the burning and fracture processes. It is apparent that the combustion/fracture coupled mechanism creates a large specific surface area for burning; and hence a real rocket motor may be highly susceptible to failure under these conditions.

(3) The dimensionless parameters deduced from the analysis outlined above provide some guidelines as to the cause and effect relationship of the energy input to a propellant sample with included flaws and the resultant damage produced in the sample. The functional form of the governing dimensionless parameter (Π_g) has been determined. It depends strongly upon the igniter strength, the chamber pressurization rate and the fracture energy of the propellant. These dimensionless parameters can be used to define safe operating domains of rocket motors with propellant grains containing cracks.

III. IGNITION OF NITRAMINE-BASED COMPOSITE PROPELLANTS UNDER RAPID PRESSURIZATION

3.1 Motivation and Objectives

Most of the solid propellant ignition studies conducted in the past were concentrated on AP-based composite propellants and homogeneous propellants. Recently, a great deal of interest has been focused on the study of nitramine-based composite propellants[2,12]. The use of nitramine fillers in composite propellants offers many advantages in rocket motors and artillery propulsion systems. High specific impulse is obtained due to the combination of high energy and low molecular weight of combustion product gases. Since the product gases are halogen-free and contain less water vapor and carbon dioxide, the smoke and infrared emissions from exhaust gases are reduced. For nitramine weight percentage below 90, nitramine composite propellants exhibit lower flame temperature than those of AP-based composite propellants. This helps to alleviate the problem of material erosion caused by highly corrosive combustion product gases. The excellent thermal stability of RDX and HMX makes nitramine-composite propellants the best candidate for Low Vulnerability Ammunition (LOVA) propellants.

Studies on nitramine propellants are mostly devoted to the steady-state burning rate experiments and thermal decomposition of pure nitramines. The ignition of nitramine propellants was studied by DeLuca et al.[13-14] experimentally using arc-image furnace and CO_2 laser. The effects of propellant formulation on ignition delay have been studied by

using various propellants (AP- or HMX- composite, and homogeneous propellants). They found that nitramine (HMX) based composite propellant is harder to ignite than AP-based composite or homogeneous propellants. Birk and Caveny[15] used a shock tunnel to determine the site and mode of convective ignition of propellant cylinders in crossflows. They also found that nitramine propellants are more difficult to ignite under transient flow conditions than single-base, double-base, or triple-base propellants. The site of the most luminous zone was found to occur at some downstream station from the stagnation point. This indicates that the ignition mechanism is mostly gas-phase reaction dominated processes rather than the surface reactions.

Isom et al.[16] determined the compositions of the pyrolysis products of a nitramine propellant and HMX crystal to examine pre-combustion reactions which are important in ignition analysis. A CO_2 laser was used to pyrolyze the samples and the pyrolyzed gaseous species were determined by molecular beam mass spectrometry. They found that at atmospheric pressure, the gaseous product species are fairly stable except HCN. As pressure increased, reactions have been promoted. They estimated rate constants for describing the combustion by a single-step reaction in the gas phase and a separate single-step reaction for the surface reaction zone. The rate constants estimated are not for the Arrhenius type rate equation. However, they suggested that the Arrhenius parameters A and E can be deducted from ignition delay and burning rate data.

To achieve understanding of mechanisms involved in the pre-combustion reactions, extensive studies have been conducted on the thermal decomposition of cyclic nitramines, especially HMX and RDX. Schroeder[17-20] collected various data and reviewed different mechanisms proposed for thermal decomposition of nitramines. Boggs[21] surveyed the literature describing the physical properties, sublimation, decomposition, ignition, and self-deflagration of RDX and HMX, and has made an excellent summary of the thermal behavior of nitramine ingredients. Fifer[22] presented a detailed review of the ignition and combustion chemistry of the nitrate ester and nitramine propellants. Extensive discussions on kinetics of NC, HMX, and RDX decomposition, catalysis of nitramine propellants, and flame-zone chemistry were presented by Fifer[22].

Kraeutle[23-25] conducted a series of studies on the thermal decomposition of HMX in the form of solid and liquid phases by isothermal and nonisothermal heating methods. The qualitative features of HMX decomposition were observed by hot stage microscopy and scanning electron microscopy. Temperature dependence of decomposition rates at atmospheric pressure was determined by isothermal weight loss measurements in the environment of various gases.

Kubota and co-workers[26-29] investigated both the thermal decomposition of nitramines and the combustion mechanisms of nitramine composite propellants. Major product species in various zones were determined by sampling probes and the thermal wave structure was studied by using microthermocouples. Most of their measurements were made for pressures

below 30 atm, since the flame zone thickness reduces significantly at higher pressures. Their scanning electron micrographs of unused and quenched RDX composite propellant sample surfaces showed strong differences[28]. The quenched sample surface showed finely divided recrystallized RDX which distributed quite homogeneously over the surface. This indicates that the RDX particles and binder must melt and diffuse into each other.

At the Pennsylvania State University (PSU), an ignition test rig has been developed to study ignition behavior of various composite propellants under rapid pressurization[12,30]. In this paper, the previously developed ignition test apparatus was modified to study the ignition characteristics of various RDX-based composite propellants.

The specific objectives are: 1) to observe the detailed gas evolution and ignition phenomena of nitramine composite propellants and gain deeper understanding of ignition processes; 2) to study the effect of pressurization rate ($\partial P/\partial t$) on ignition delay as partially signified by the delay of light emission; 3) to compare ignition behavior of a series of RDX-based composite propellants with different binders; 4) to consolidate from piecewise information of nitramine decomposition and pyrolysis behavior into an overall picture of the ignition processes of nitramine propellants; 5) to propose a reaction mechanism which governs the ignition processes; and 6) to construct a unified theoretical model for the ignition of nitramine propellants.

3.2 Method of Approach

3.2.1 Test Apparatus

In the present study, the ignition test chamber developed previously[12,30] has been modified to obtain sustained ignition of the RDX-based composite propellant samples. A schematic diagram of the test section is shown in Fig. 18a. A close-up view of the cylindrical propellant sample and near-infrared photodiode is shown in Fig. 18b. Details of the test chamber and instrumentation can be found in the previous papers[12,30]. For all ignition test firings of nitramine composite propellants conducted in the previous study[12], there was only one firing in which the propellant sample attained full ignition followed by sustained burning. Other firing data represent the onset of gas evolution followed by extinction. This indicates that the previous test rig configuration could not provide a heating period long enough for propellants to establish adequate thermal layer thickness required for sustained burning. Some modifications were made to maintain high chamber pressure for a longer period of time. An auxiliary propellant charge was added at the entrance region of the channel (see Fig. 18a). The gap size of the channel was enlarged to minimize the conductive heat loss from the hot igniter gas to the walls of the flow channel, and to reduce pressure difference between the entrance and the tip of the channel.

Figure 19 shows the schematic diagram of the data acquisition system. The data acquisition system is comprised of (1) a high-speed

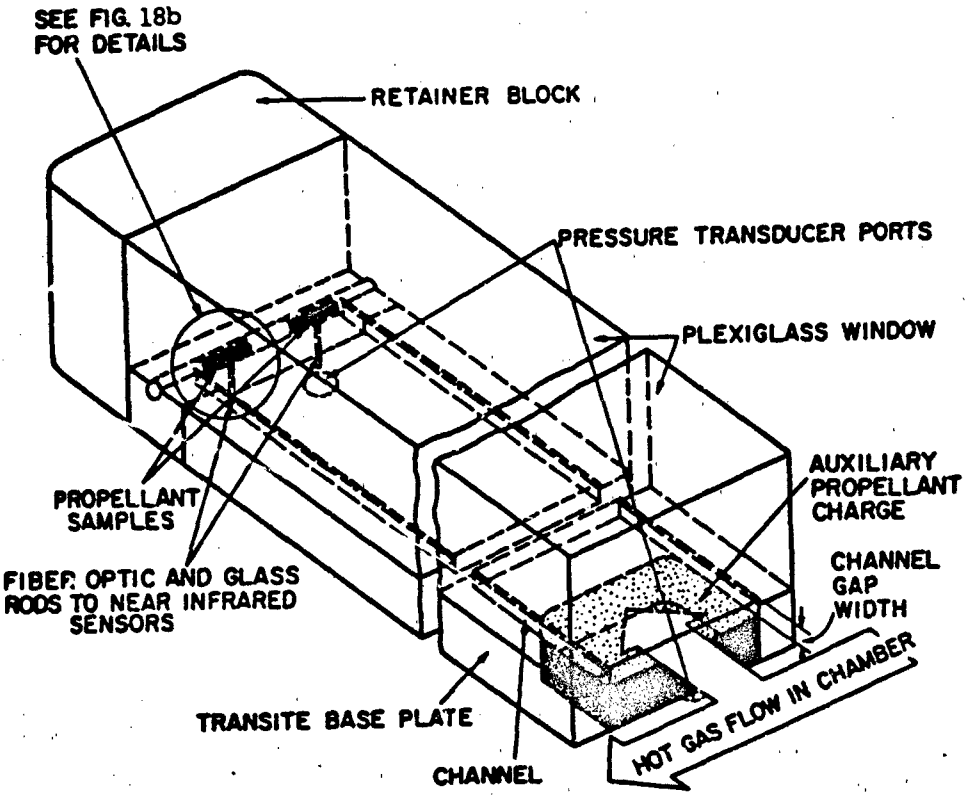

Fig. 18a Schematic Diagram of Test Section

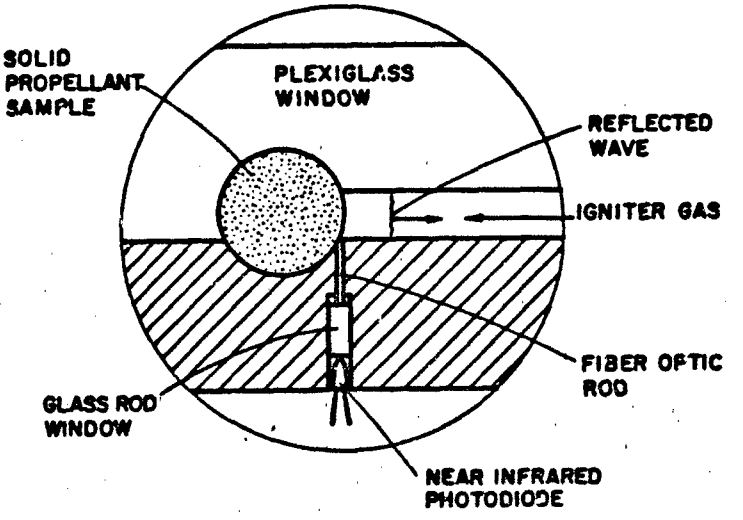

Fig. 18b Close-Up View of Cylindrical Propellant Sample and Near-Infrared Photodiode

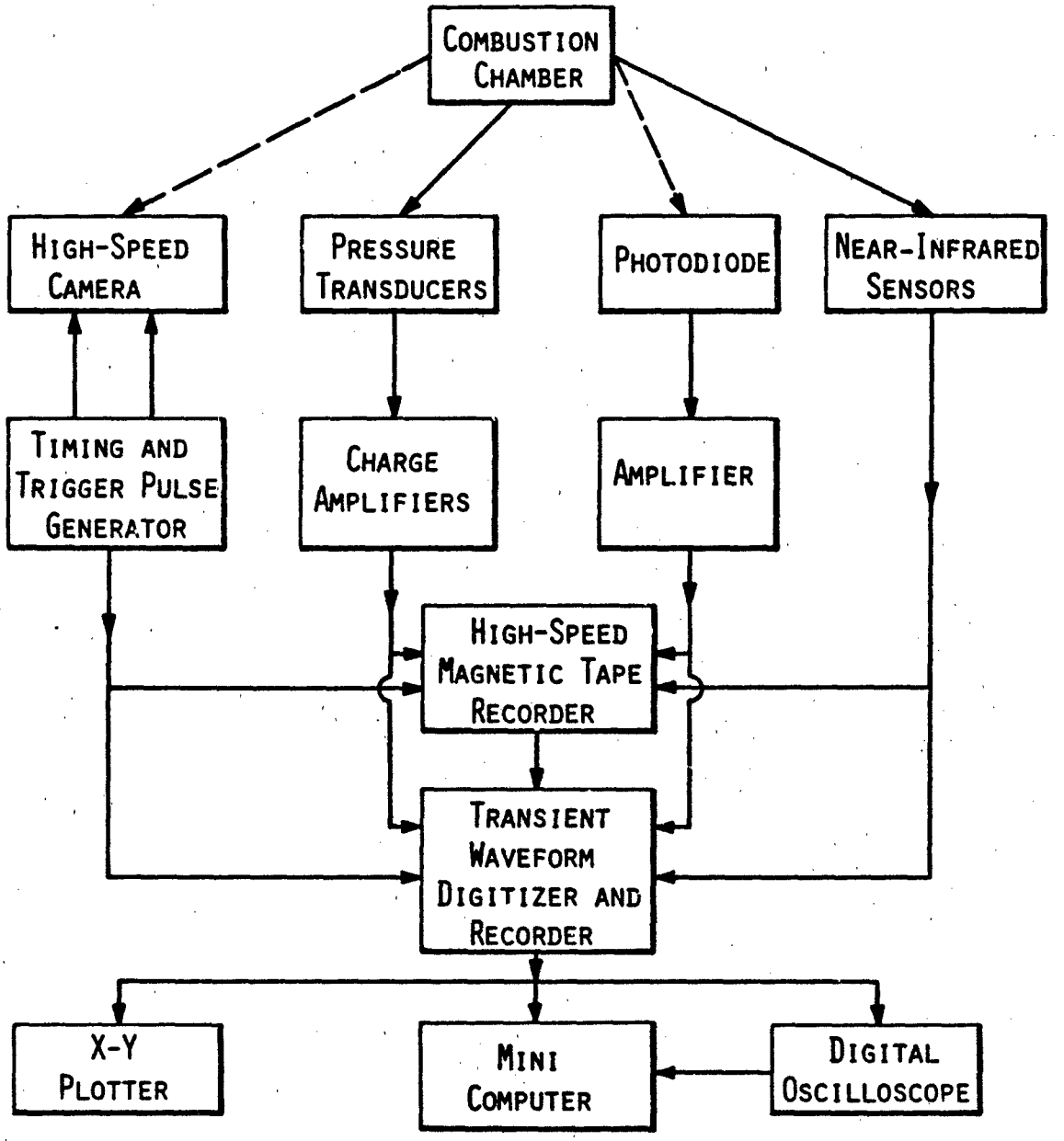

Fig. 19 Schematic Diagram of Data Acquisition System

photography system, (2) a pressure measurement system, (3) a photodiode light detection system, and (4) a near-infrared sensing system. A 16-mm Hycam movie camera is used to record the complete ignition event in the test chamber. In the pressure measurement system, signals from pressure transducers are amplified by charge amplifiers and then recorded on high-speed magnetic tape recorder and a 2 MHz transient waveform recorder. Piezoelectric quartz transducers have rise times of 1.5 μs and natural frequency of 300 KHz. The photodiode system consists of a photography lens mounted on an optical bed, a fast-response photodiode, and an amplifier. In order to observe ignition of the propellant surface, a small region around the propellant surface is focused onto the photodiode by the lens. Output of the photodiode can be amplified before recording. The near-infrared sensors are used to detect the rise of surface temperatures of the solid propellant samples. The photodiode and near-infrared detection systems are used in conjunction with the high-speed movie camera to determine the onset of light emission and ignition.

3.2.2 Propellant Samples

A series (BLX series) of RDX-based composite propellants formulated and processed at Naval Weapons Center (NWC)[32] have been used in the present experiments. One type of propellant sample was processed at Naval Ordnance Station (NOS)[33]. All of the propellants discussed in this paper are RDX-based composite propellants with different binders.

Table 2 Composition of Test Propellants

Propellant Samples / Ingredients	BLX-4	BLX-6	BLX-8	BLX-9	NOS-A
Filler	RDX (75%)	RDX (73%)	RDX (68%)	RDX (66%)	RDX (79%)
Main Binder Ingredients	TMETN GAP N-100	EHA VP DOM	GAP N-100	BTTN GAP N-100	CTPB

Table 3a Thermal and Physical Data of Major Propellant Sample Ingredients

Properties / Ingredients	Molecular Weight (Kg/Kmol)	Density (Kg/m^3)	Heat of Formation (Kcal/Kg)	Heat of Combustion (Kcal/Kg)	Heat of Explosion (Kcal/Kg)	Melting Point (C)	Vapor Pressure (Pa)
RDX	222.	1820.	66.19 ~95.9	2.285	1439.	204.	-
GAP	2455.	1300.	13.85	-4.854	-	-	-
BTTN	241.	1520.	-371.2	2.168	1420.	-27.	147
TMETN	255.	1470.	-389.	2.542	1236.	-3.0~ -17.5	.017

Table 3b Molecular Structures of Major Ingredients

INGREDIENTS	RDX	GAP	BTTN	TMETN
MOLECULAR STRUCTURE	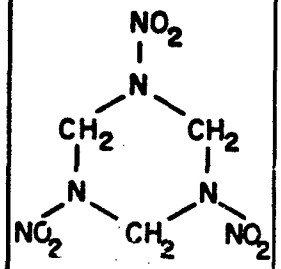	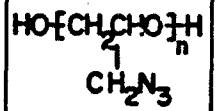	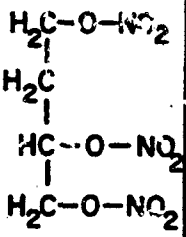	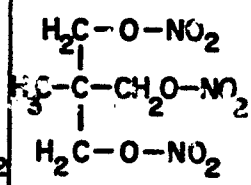

Table 2 shows the composition of test propellants. All the BLX series samples are RDX-based composite propellants with RDX weight percentage ranging from 66% to 75%. The major ingredients of BLX-4 binder system are trimethylolethane trinitrate (TMETN) and glycidyl azide polymer (GAP). The binder system of BLX-9 is also the combination of GAP and energetic plasticizer. In this formulation, TMETN has been replaced by butane triol trinitrate (BTTN). GAP is the only major ingredient of BLX-8 with about 5% of poly functional isocyanate (N-100). BLX-6 has an acrylic binder system including 2-ethylhexylacrylate (EHA), N-vinyl-2-pyrolidane (VP), and dioctylmaleate (DOM). NOS-A has a carboxyl terminated polybutadiene (CTPB) binder system.

The thermal properties and physical data of RDX and other ingredients used in various binder systems are given in Table 3a. The molecular structures of major ingredients are given in Table 3b.

3.3 Physicochemical Considerations for Pyrolysis and Ignition of Nitramine Propellants

3.3.1 Description of Physical and Chemical Processes

Thermophysicochemical processes involved in the ignition and combustion of nitramine composite propellant are described below. Figure 20 shows a general diagram composed from various studies of nitramine propellant decomposition, ignition, and combustion. It is evident that the ignition and combustion of nitramine composite propellants involve

Fig. 20 PHYSICAL AND CHEMICAL PROCESSES IN THE IGNITION AND COMBUSTION OF NITRAMINE COMPOSITE PROPELLANTS

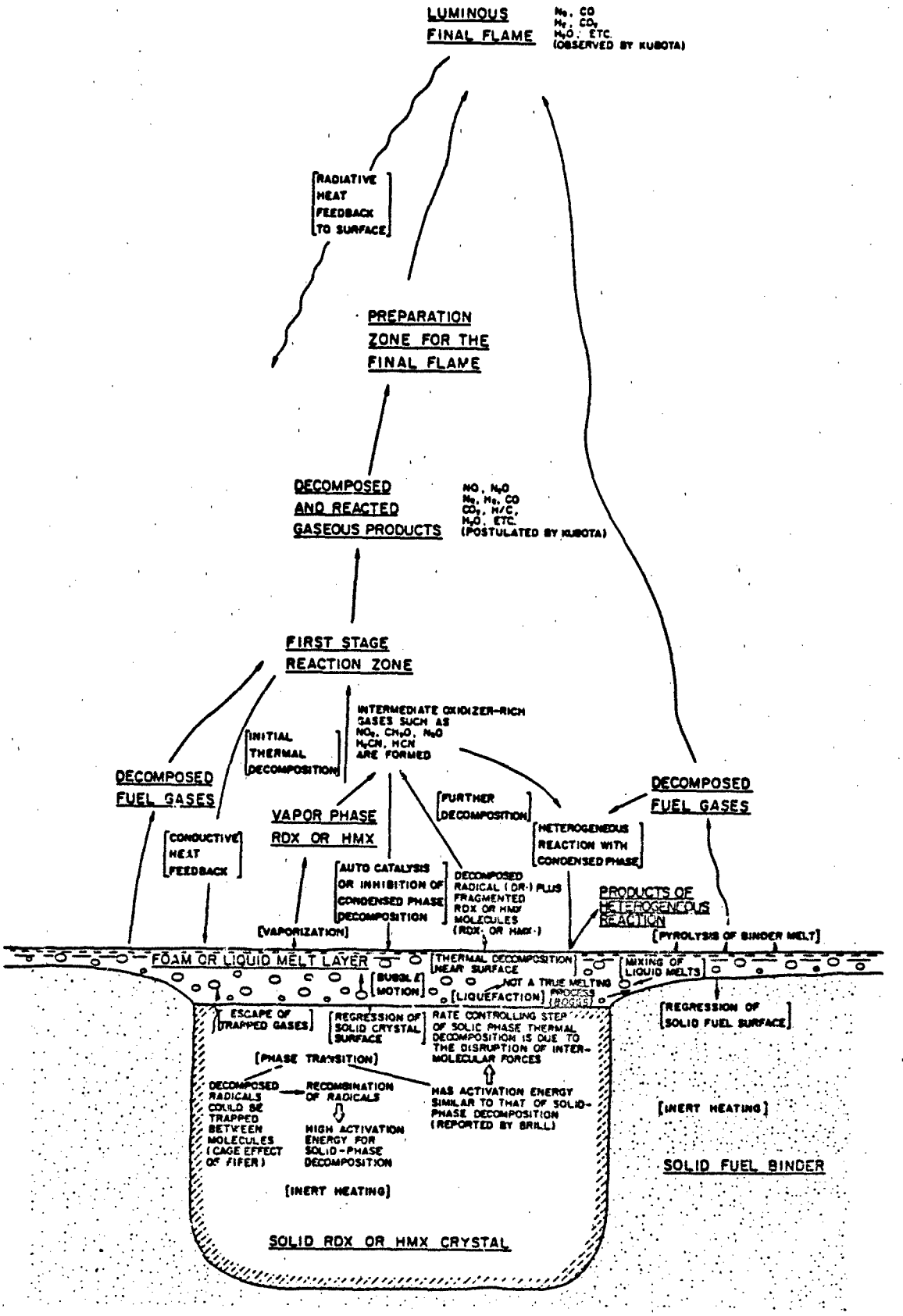

many intricate physical and chemical processes. When heated by ambient gases, the solid-phase nitramine crystal and binder undergo inert heating in the subsurface region. Near the surface of nitramine crystal, phase transition may occur. Decomposed radicals could be trapped between molecules or within molecules. This produces the so-called "Cage Effect" proposed by Fifer[34]. Trapped radicals can recombine due to their close proximity and low mobility[34]. This recombination process is generally believed to be the reason for higher activation energy in solid-phase decomposition than those of liquid and gas phases[34]. It was reported by Brill[35] that the phase transition has activation energy similar to that of solid-phase decomposition. He postulated that the rate controlling step of solid-phase thermal decomposition is due to the disruption of intermolecular forces.

At the interface between the gas phase and condensed phase, a foam or liquid melt layer could be formed above the solid phase crystal and binder. The foam layer may contain various sizes of bubbles. The melt layer of the nitramine filler could be formed at a temperature lower than the melting point of pure nitramine. This phenomenon is considered as liquefaction by Boggs[21]. Boggs stressed that liquefaction is not a true melting process. Melt of nitramine filler and binder could be mixed to form an energetic melt layer. Vaporization of liquid melt can occur on the surface of the melt layer. In the meantime, thermal decomposition of the nitramine filler in the liquid phase can yield decomposed radicals and fragmented nitramine molecules in the initial decomposition step. Further decomposition of the gaseous species formed at the initial

step and vapor-phase decomposition will yield slightly oxidizer-rich gases. Some of the gaseous species from the oxidizer-rich gases could attack the surface of the melt layer. Chemical species of the oxidizer-rich gases will react with each other exothermically to form the first stage reaction zone. Before reacting in the final flame, the gaseous products from the first stage reaction zone may pass a preparation zone where reaction kinetics are retarded. The gaseous species from the preparation zone and the decomposed fuel gases will react eventually to form the final luminous flame.

Radiative heat could be transferred from the luminous final flame to the first reaction zone and the foam or melt layer. Simultaneously, the conductive heat feedback to the condensed-phase surface will occur near the first reaction zone. The mechanisms depicted in Fig. 20 are based upon observations and physical understanding of ignition and combustion processes.

3.3.2 Thermal Decomposition of Nitramines

Since it has been considered that the overall chemical processes in deflagration of nitramine composite propellants are dominated by thermal decomposition of pure nitramine, extensive studies have been conducted on the subject. Schroeder[17-20], Boggs[18], Fifer[22], Dubovitskii and Korsunskii[36], and McCarty[37] reviewed the literature on the kinetics and reaction mechanisms of the thermal decomposition of nitramines, especially RDX and HMX. Despite the extensive studies on the thermal

decomposition of RDX and HMX, the detailed mechanisms are generally unknown. Even the initial step(s) of the reactions is controversial.

Various mechanisms proposed have been critically reviewed by Schroeder[17-20]. An excellent arrangement of the probable mechanisms has been prepared by Shaw and Walker[38]. The main question concerning the primary step (or steps) of thermal decomposition of RDX and HMX is whether it is N-N bond fission or C-N bond cleavage. Fission of $N-NO_2$ bond has been generally considered as an initial step of the decomposition mechanism of RDX and HMX. Growing evidence is shown for C-N bond cleavage, mostly by mass spectroscopic[39,40] and labelling studies accompanying rapid pyrolysis[41]. The initial decomposition schemes are: (1) elimination of CH_2NNO_2, (2) $N-NO_2$ fission, (3) homolytic C-N cleavage, (4) HONO elimination, (5) concerted depolymerization to 4 CH_2NNO_2, and (6) transfer of an oxygen atom from an $-NO_2$ group to a neighboring $-CH_2$ group.

A mechanism proposed by Karpowicz, Gelfand and Brill[35] is quite different from those of covalent bond cleavage. Based on observation of their phase transition experiments, it was proposed that disruption of intermolecular electro-static forces, rather than covalent bond cleavage, is what controls the rate of thermal decomposition of HMX. As mentioned above, Fifer also postulated the "Cage Effect"- an induced recombination of radicals generated in the initial dissociation step. He suggested that cage escape (the escape of decomposed gaseous species from condensed region) might be rate controlling for the

condensed-phase decomposition. In general, both Fifer and Brill consider intermolecular actions to be dominant factors in condensed-phase decomposition.

3.3.3 Kinetic Model

The kinetic model presented in this study is somewhat similar to that proposed for AP-based composite propellant ignition model developed by Kuo and coworkers[31]. Detailed description of the mathematical model can be found in Ref. 31. The reaction mechanisms used in the present model can be extended to include various initial decomposition mechanism discussed previously. The initial step can be N-NO_2 fission, C-N bond cleavage, HONO elimination, or other mechanisms.

The present investigation considers the following five representative chemical reactions: 1) vaporization of nitramine filler followed by thermal decomposition to form oxidizer-rich gases, 2) initial thermal decomposition of liquid phase nitramine to form decomposed radicals (DR°) and fragmented RDX(RDX°), 3) further decomposition of RDX° to form intermediate oxidizer-rich gases which then react in the first-stage reaction to form $Ox_{(g)}$, 4) binder pyrolysis to form fuel-rich gases, and 5) reaction of $Ox_{(g)}$ and $F_{(g)}$ to form final products in the luminous flame:

$$RDX_{(\ell)} \xrightarrow[\text{vaporization}]{k_{1a}} RDX_{(g)} \xrightarrow[\text{decomposition}]{k_{1b}} Ox_{(g)} \qquad \text{Reaction 1}$$

$$RDX_{(\ell)} \xrightarrow[\substack{\text{initial thermal}\\ \text{decomposition}}]{k_2} DR^{\cdot}_{(g)} + RDX^{\cdot}_{(g)} \qquad \text{Reaction 2}$$

$$DR^{\cdot}_{(g)} + RDX^{\cdot}_{(g)} \xrightarrow[\substack{\text{further}\\ \text{decomposition}}]{k_{3a}} \underset{\substack{\text{oxidizer-rich}\\ \text{gases}}}{\text{intermediate}} \xrightarrow[\substack{\text{first-stage}\\ \text{reaction}}]{k_{3b}} Ox_{(g)} \qquad \text{Reaction 3}$$

$$\text{Binder}_{(\ell) \text{ or } (s)} \xrightarrow[\text{pyrolysis}]{k_4} F_{(g)} \qquad \text{Reaction 4}$$

$$Ox_{(g)} + F_{(g)} \xrightarrow[\text{final flame}]{k_5} \text{Products}_{(g)} \qquad \text{Reaction 5}$$

Depending upon the options considered for radical initiation, DR$^{\bullet}$ could represent $NO_2^{\bullet}$, $CH_2NNO_2^{\bullet}$, HONO$^{\bullet}$ or any other reactive species. Some of the kinetic data required as input for the thermal decomposition of nitramine filler are available from various decomposition experiments. Other kinetic constants such as k_5 required for the above reaction model must be based upon the kinetic data of similar reactions. Part of these required kinetic data are summarized in Ref. 2. In view of the fact that not all required chemical kinetic constants are known, no numerical results are presented in this paper. Experimental results and observations are discussed in the following section.

3.4 Results and Discussion

Series of test firings were conducted to determine the onset of light emission and sustained burning of propellant samples under various pressurization rates. The peak pressures achieved in the test firings are in the range of 10.34 to 27.58 MPa (1500 to 4000 psi). The general shape of the pressure trace near the propellant sample location can be divided into three regions: 1) an uprising pressurization region; 2) a region of maximum pressure achieved; and 3) a depressurization region. In order to measure the time required for onset of light emission, t_{LE} from the propellant sample, the initial zero time in the present study is defined as the first discernible pressure rise at the entrance of the flow channel.

The sequence of events that occur during the test can be described as follows. Hot combustion product gases from the igniter system flow into the main test chamber and pressurize it. The pressure gradient causes a part of gases to penetrate into the narrow channel formed between the transite base plate and the plexiglass window. As pressurization of the channel begins, temperature in the channel increases and the gases flow toward the channel tip at high velocities. Hot gases and the front of pressure wave propagate along the channel, reach the tip, and reflect from the closed end. The ignition product gases in the reflected region could react further to release heat in the local region. A part of the heat released could be fed back to the solid propellant sample. As the process continues, additional hot gases are driven into the channel due to the continued rise of chamber pressure. Following a period of inert heating, the mechanisms described above for ignition and combustion will occur. Finally, high rates of gas-phase chemical reactions result in onset of light emission.

For the test reported in this paper, pressure measurements were made at two locations along the channel; one at the entrance of channel and the other near the sample location (see Fig. 18a). The onset of emission of luminous light near the propellant surface is determined by first locating the event on the film, and then by comparing it with the photodiode and near-infrared sensor signals.

A typical set of time-correlated data is shown in Fig. 21. This figure includes a trigger pulse (common time signal), two near-infrared sensor signals (NI1 and NI2), a photodiode signal (PD), a P-t trace near

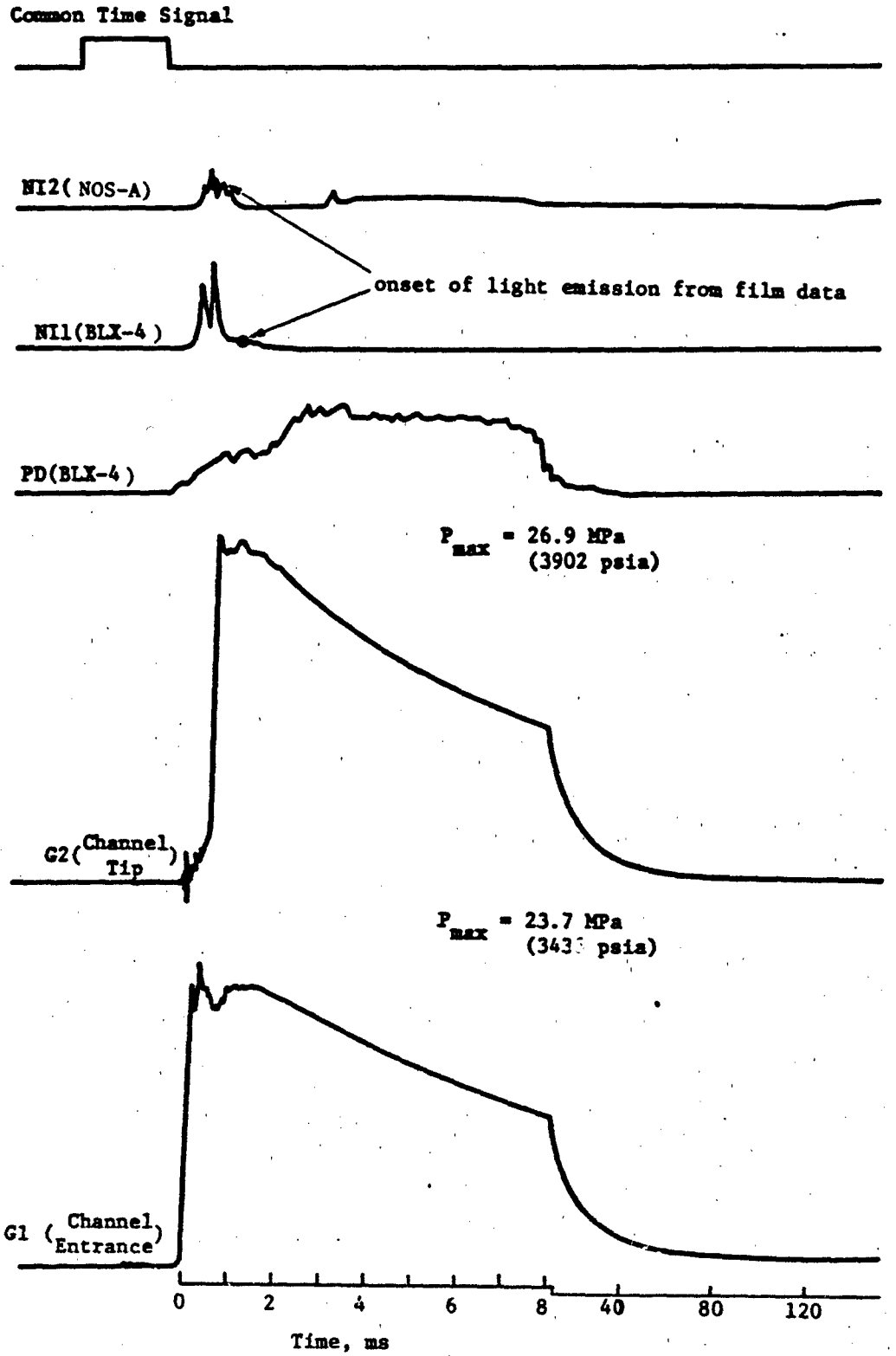

Fig. 21 Typical Set of Time Correlated Data of Nitramine Propellants Ignition Test Firing

the channel tip (G2), and a P-t trace at the channel entrance (G1). The trigger pulse is generated by a light-emitting diode (LED) driver unit, and is used to correlate time between data obtained from high-speed movie films and those recorded on transient wave form recorder. A dual time base is used in this test to capture the complete ignition event while giving high time resolution in the most interested time period. By this arrangement, the initial portions of the recorded signals are expanded to illustrate the time variation of pressurization, light emission, and sample surface temperatures. The time delay between the first discernible pressure rise at the tip and that of the entrance is caused by the finite time required for the pressure front to propagate from the entrance to the tip during initial pressurization. Except for a short period immediately following the arrival of the pressure wave front at the tip, the average pressurization rate is generally lower near the tip, resulting from frictional losses in the channel as hot gases travel to the closed end.

As shown in Fig. 21, both near-infrared sensors and photodiode give a rapid rise signal slightly after the pressure rise at the tip. These signals are compared with the information obtained from the film before determining the time for onset of light emission from the propellant surface. Although the consistency between these three independent measuring devices is very helpful in interpreting the data and in reducing unnecessary errors, it is not always possible to obtain totally consistent information. For example, the near-infrared sensor NI1 of this test yielded very inconsistent information on t_{LE}. This is prob-

ably due to the undersized effect of the BLX-4 propellant sample. As can be seen from Fig. 18b, if the sample size is slightly smaller than the cylindrical cavity designed for the sample, the hot gases from the ignition can easily trigger the near-infrared sensor due to mechanical displacement of the sample surface by gas compression. The rapid decay of NI1 signal after the peaks could be by the deposit of soot particles on the end surface of the fiber optics rod. After analyzing the motion picture films, the onsets of light emission from two propellant samples are designated on the near-infrared and photodiode signals as black dots shown in Fig. 21. In this particular case, the NOS-A propellant begins to emit light slightly sooner than the BLX-4 propellant. The propellant samples in this particular firing were partially burned.

Figure 22 shows a comparison of the measured times for the onset of light emission of different propellant samples under various pressurization rates. These five different propellants have different kinds of binders as discussed previously. The figure clearly demonstrates the general trend that the time required for the onset of light emission decreased as pressurization rate increases for all type of propellants except BLX-6. The data of BLX-6 propellant are scattered and more experiments are needed for this propellant to identify the trend of dependence of t_{LE} on $\partial P/\partial t$. The figure also shows that the ease of obtaining first light emission increases in the following order: NOS-A, BLX-4,BLX-9 BLX-8. However, this order does not provide information about the ease of ignitability of the propellant samples. From the recovered partially burned samples, it appears that sample NOS-A is the most

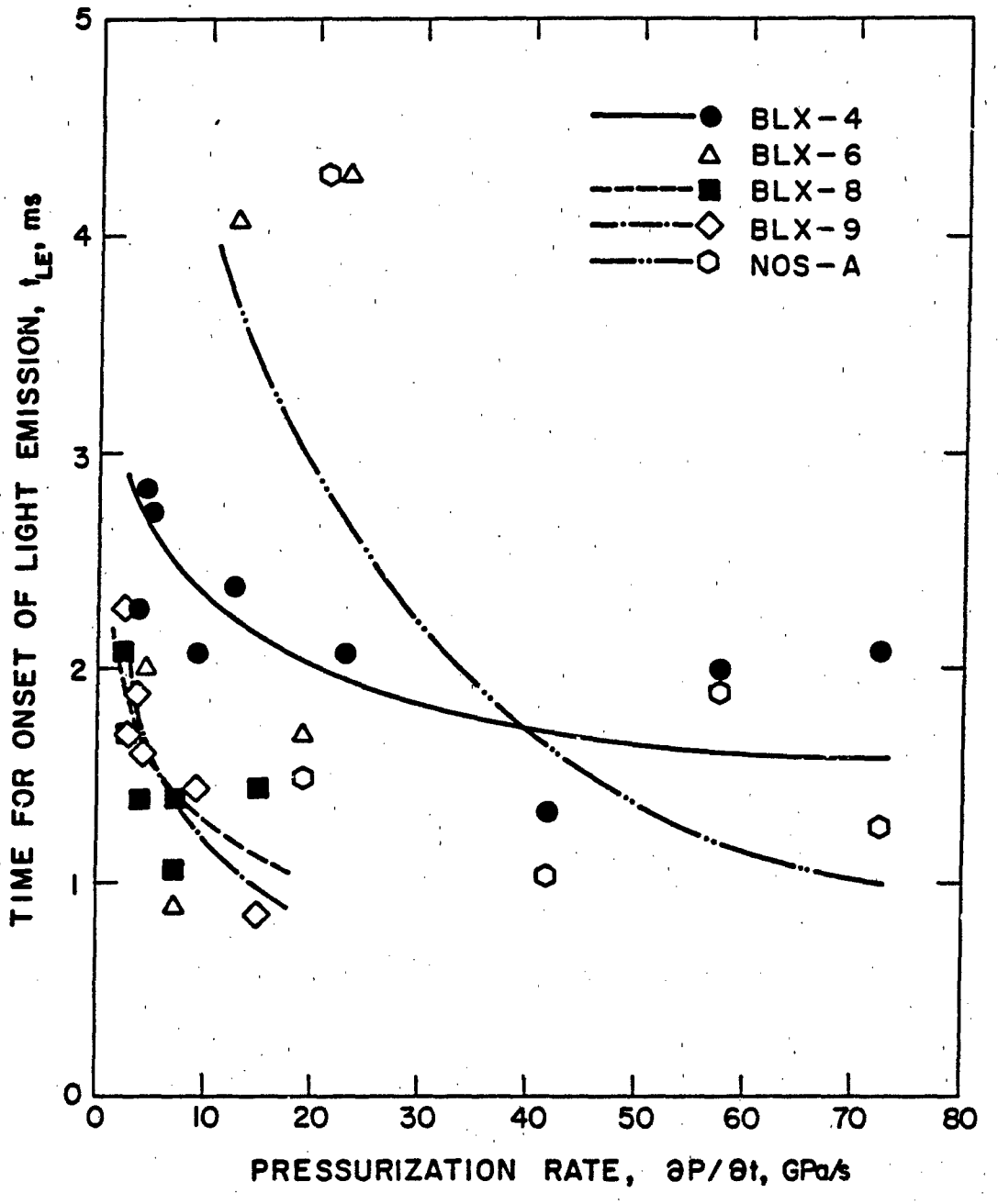

Fig. 22 Time for Onset of Light Emission as a Function of Pressurization Rate

vulnerable propellant among all the samples tested, whereas BLX-6 is the least vulnerable.

In almost all of the test firings conducted on BLX-6, this sample was practically unburned or only slightly burned. Sample BLX-6 is a plastic bonded explosive and does not contain energetic plasticizer; it is expected that this sample has poor burning properties. BLX-4 and BLX-9 both contain RDX as oxidizer and GAP binder, but have different energetic binders. BLX-4 contains TMETN as binder whereas BLX-9 has BTTN. Both of these energetic binders have very similar physical properties. Experiments show that BLX-4 and BLX-9 do have similar ignitabilities in terms of sustained burning. When comparing BLX-8 with BLX-4 and BLX-9, results show that BLX-8 has a lower degree of ignitability. This is reasonable since BLX-8 is a pure GAP propellant without energetic binder, as opposed to BLX-4 and BLX-9 which have energetic binders. As mentioned above, the time for onset of light emission from propellant surface does not really provide information concerning the vulnerability of the propellant. It implies that propellant samples with shorter t_{LE} do not necessarily show higher mass consumption. This indicates that propellant vulnerability should be evaluated by both t_{LE} and the amount of mass consumed.

The decrease in t_{LE} with increasing pressurization is believed to be caused by enhanced heat feed back to the propellant surface at higher pressurization rates. This augmentation in heat feedback to the propellant at higher pressurization is a result of a combination of the following mechanisms: heating due to compression-wave reflection at the

closed end; heat transfer due to recirculating hot gas near the tip, behind the reflected compression wave; and increase in temperature of the gas adjacent to the propellant surface due to continued pressurization of the channel cavity.

A scanning electron microscope (SEM) was used to investigate the surface structure of the test samples both before and after the ignition tests. Figures 23 and 24 show the surface structures of the test samples (BLX-6 and BLX-4) before and after the ignition tests. The pretest photograph of the surface structure of BLX-6 sample indicates that the filler particles on the surface were covered with binder materials. This

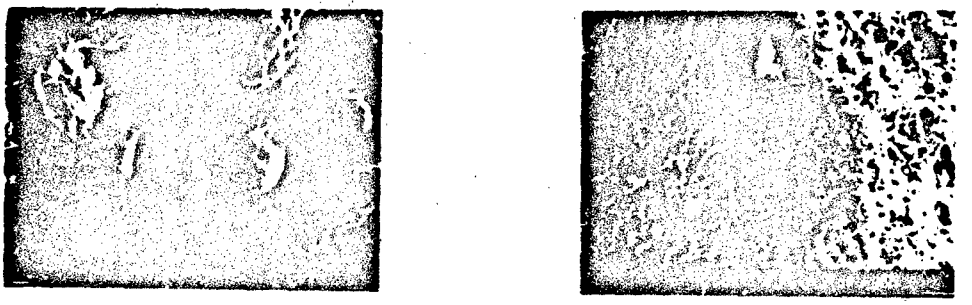

(a) Before Test (b) After Test

Fig. 23 Micrograph of Sample Surface Structure (BLX-6)

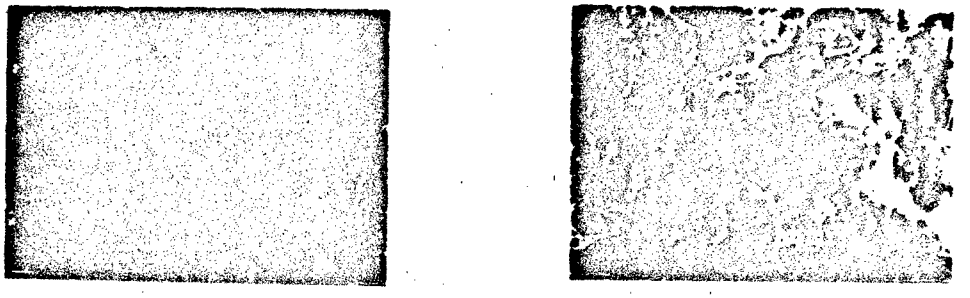

(a) Before Test (b) After Test

Fig. 24 Micrograph of Sample Surface Structure (BLX-4)

covering could possibly delay the ignition processes and may explain the low ignitibility of BLX-6 samples. On the contrary, the pretest sample of BLX-4 propellant showed no such coverage, and hence it can be ignited more easily.

3.5 Conclusions on Ignition Studies of Nitramine-based Composite Propellants under Rapid Pressurization

Some important observations and conclusions can be summarized as follows: 1) observed ignition phenomena of various types of RDX-based composite propellants and found the time for onset of light emission (t_{LE}) decreases as pressurization rate ($\partial P/\partial t$) increases; 2) t_{LE} depends strongly on propellant ingredients and their mass fractions; 3) propellant samples with shorter t_{LE} do not necessarily show higher mass consumption, indicating that propellant vulnerability should be evaluated by both t_{LE} and the fraction of mass consumed; 4) a unified kinetic mechanism has been proposed for nitramine propellant ignition; and 5) in order to test the validity of the proposed model, more kinetic data are needed.

IV. IGNITION OF NITRAMINE-BASED COMPOSITE PROPELLANTS BY CO_2 LASER

4.1 Background and Motivation

Radiative ignition techniques have been used widely for research and testing of ignition properties of newly formulated propellants. Before the development of CO_2 lasers, the arc image furnace was the most popular radiative ignition device. However, many problems were associated with the use of an arc image furnace, including relatively low energy fluxes for simulating conditions in actual rocket motors and gun propulsion systems, nonuniform heating which caused local subsurface hot spots, inefficient heating which generated thicker thermal waves at propellant surface due to in-depth absorption, and the possibility of introduction of photochemical reactions. As a result of low energy fluxes, the sample must be placed so close to the focal point which is located at a short focal distance from the parabolic mirror that complicated geometric effects in the radiative ignition study are introduced.

In the last decade, laser technology has developed to the extent that the laser is now an attractive alternative device to the arc image furnace. Use of a high-powered CO_2 laser, in particular, has dealt with many of the problems associated with the arc image furnace. For example, the high intensity of a CO_2 laser permits propellant test samples to be irradiated effectively with a parallel beam, and helps to avoid the various geometric complexities that accompany use of the very small F-number systems needed to obtain adequate fluxes from an electric arc.

The monochromatic characteristics of a laser beam also alleviate the complexities involved with many absorption coefficients which vary with wavelength. Because low quantum energy of a CO_2 laser is about one order of magnitude less than the energy of chemical bonding in samples, photochemical effects are largely excluded.

A CO_2 laser is especially useful as an energy source in heating samples to produce pyrolyzed gases. These gases are then analyzed to determine pyrolysis mechanisms, which are very important in understanding the mechanisms and in modeling solid propellant ignition and combustion. The use of a CO_2 laser in studying ignition is not totally ideal due to several minor drawbacks. These include (1) in-depth absorption and scattering of radiative energy fluxes, (2) interaction of the laser beam with pyrolyzed gaseous products, and (3) spatial nonuniformity of the radiative energy flux. These difficulties do not necessary destroy the usefulness of the technique; for example, the spatial nonuniformity can be eliminated by using laser beam devices, such as a kaleidoscope. Furthermore, due to the long wavelength of a CO_2 laser, most of the CO_2 laser energy is absorbed in the region near the surface of the sample.

Ohlemiller and Summerfield[43] used a CO_2 laser to study radiative ignition behavior of a heterogeneous system (with special reference to solid propellants), and to clarify certain aspects of the effect of radiation on the observed behavior. Polystyrene and an epoxy polymer in oxygen/nitrogen mixture were studied. Ignition delay time was measured as a function of radiant flux, pressure, oxygen percentage, and absorp-

tion coefficient of the fuel. They found that the radiative ignition of a pure fuel in an oxydizing gas is much slower than ignition by an identical heat flux applied by a hot gas source. Two main reasons for the retardation were summarized: (a) the radiative transparency of the fuel results in slower surface heating, and (b) the cool gas environment in the usual radiation ignition test rig suppresses the incipient ignition.

Saito et al.[44] studied the ignition of composite propellants by means of a CO_2 laser under subatmospheric pressure. They devised a means to intermingle the coherent rays emitted from a laser tube with two oscillating polished flat reflectors. They found that the ignition site of a laminated propellant composed of an AP crystal and a CTPB slab was located near the interface between AP crystal and CTPB binder, and on the AP surface when a far-infrared beam of CO_2 laser was irradiated at low heat flux (<7 cal/cm^{2}sec) and low pressure (<100 torrs). They also reported that a helium environment provided remarkably longer ignition time compared with an environment of Ar and N_2 gases. Harayama et al.[45] used a composite propellant as a sample which is embedded with fine-wire thermocouples. On the plot of pressure versus incident heat flux, they divided the ignition map of the composite propellant into four zones: (1) the self-sustaining ignition zone at high pressures and heat fluxes, in which stable combustion is followed spontaneously; (2) the non self-sustaining ignition zone at lower pressure ranges, in which the sample extinguishes after the laser beam is cut off; (3) the pulsating ignition zone at lower incident heat fluxes, in which the propellant

burns in an oscillatory manner with repeated ignition and extinction processes induced by the delay of the decomposition and surface pyrolysis; and (4) no ignition zone at either extremely low pressure or low heat fluxes. They emphasized the non self-sustained mode of ignition of AP/CTPB composite propellants, and defined the boundary of this zone as a function of pressure and radiant heat flux. In terms of exposure time versus incident heat flux plot, the boundary between non self-sustaining ignition zone and no ignition zone is demarcated by the minimum exposure time which decreases with the increase in incident heat flux. The boundary line between self-sustaining and non self-sustaining zones is almost vertical at a critical heat flux (boundary irradiative intensity) below which self-sustained ignition is observed. They concluded that the non self-sustaining ignition mode exists at the low pressure and high irradiative intensity region. On generating the incipient flame, the sub-surface temperature profile for the non self-sustaining ignition becomes steeper than that for the self-sustaining mode. For aluminized propellants, the ignition delay time is longer, and the boundary irradiative intensity between the self- and non self-sustaining ignition modes is higher than that for non-aluminized propellants. The ignition modes were controlled mainly by the temperature profile at the instant of the incipient flame appearance.

Cook[46] applied CO_2 laser for ignition studies. He used a laser ignition setup to test the relative ignitability of various grains and to monitor formulation variables of LOVA propellants. The evaluation of ignitability was based on ignition delay, heat flux, and total ignition

energy. Several environmental parameters, such as pressure, temperature, and gas composition, were varied. Several sample sizes and sample orientations were also considered. The optical properties of samples were determined by a specially designed optical property analyzer using an integrating cone concept.

Kashiwagi[47] studied radiative ignition of polymethylmethacrylate (PMMA) and red oak using a CO_2 laser with incident flux up to 20 W/cm^2. Strong attenuation of the incident laser radiation by the gaseous plume evolved from the horizontal sample surface was observed. It is postulated that, under autoignition, PMMA ignites through the absorption of incident radiation by the decomposition products in the gas phase. In a subsequent work, Kashiwagi[48] studied the effect of sample orientation on auto ignition delay time. He concluded that ignition delay times were shorter with the horizontal sample than with the vertical sample at the same external radiant heat flux, since the decomposed gaseous products above the horizontal sample absorb more radiant energy to achieve ignition.

Kashiwagi[49] used a high-powered CW CO_2 laser (max heat flux = 5000 W/cm^2) to obtain a fundamental understanding of the ignition mechanism of a liquid fuel (n-decane). The events from the preheating period through ignition were recorded by high-speed photography. Kashiwagi studied the effect of the container size and determined the appropriate size to avoid wall effects. He also studied the effect of incident angle (between the beam axis and the liquid surface) on ignition, and found that upon reduction of the incident angle the ignition delay time

becomes longer and the minimum incident flux for ignition increases significantly. He proposed that the autoignition mechanism of the liquid fuel by a CO_2 laser is the absorption of the incident laser beam energy by the plume of fuel vapor.

Kashiwagi and his co-workers[50] successively used the CO_2 laser adjusted at a relatively low energy heat flux (about 1000 W/cm^2) to study the ignition mechanism of liquid fuels under radiative heating. Three parameters (laser flux, incident laser angle with respect to the liquid surface, and absorption coefficient of the liquid) were varied. The phenomena in the vicinity of the liquid fuels were observed by both high-speed schlieren and direct photography. In time sequence, the pictures revealed the formation of a radial wave on the liquid surface, a central surface depression, bubble nucleation, growth, and bursting, followed by complex surface motion, further bubbling, and ignition of fuel vapor. An order of magnitude analysis was developed to interpret the phenomena. Based upon their studies, it is concluded that the differences in absorption coefficient between the different liquid fuels and their vapors have a major effect on ignition delay time.

Mutoh et al.[51] explored the behavior of the radiative ignition of PMMA by examining the ignition delay and the temperature and fuel concentration distributions in the gas phase during ignition. A CO_2 laser was used as the energy source. A Mach-Zehnder interferometer was employed to determine the temperature and fuel concentration distributions. They found discontinuity in the ignition delay time at a certain critical radiant flux. For a radiant flux beyond the critical value,

ignition occurs at the plume axis away from the sample surface; however, for a radiant flux below the critical value, ignition occurs near the sample surface close to the plume boundary. The ignition mechanism changes from gas-phase to heterogeneous reaction as the incident radiant energy flux is reduced from a level above the critical value to a lower level than critical.

Beckel and Matthews[52] used a CO_2 laser as an ignition source to investigate the effects of ignition source intensity, oxidizer flow rate, and oxidizer composition on the ignition of PMMA. They used a He-Ne laser/photodetector servomechanism feedback system to hold the surface of the sample at a specified position. An opposed flow diffusion flame system supplied oxidizer gas flow perpendicular to the sample surface. In this arrangement, a stationary diffusion flame is established at a certain standoff position from the fuel sample. They found that the polymer surface temperature at ignition is independent of source intensity, oxidizer composition, and oxidizer flow rate. They also found that the ignition delay time is independent of oxidizer velocity over the range of velocities as long as a flat flame can be established in the test rig. The gas-phase absorption of radiation, however, could affect the ignition process significantly even for relatively small optical depths and at low-energy source intensities.

Using a CO_2 laser, Isom et al.[16] determined the composition of the pyrolysis products as a function of distance from the surface of a crosslinked double-base (XLDB) propellant, HMX, or an energetic binder containing nitroglycerin. They emphasized precombustion reactions,

which are important in transient combustion problems. The pyrolized gas was analyzed by molecular beam mass spectrometry. Realistic pressures ranging from atmospheric to 1.379 MPa (200 psi) were used in the pyrolysis experiment. They found that at atmospheric pressure the propellant product composition remained fairly constant with distance except for HCN. At 1.379 MPa (200 psi), the propellant reactive species (HCN, NO) were consumed within a short distance. At atmospheric pressures, the HMX ring fragment C_2H_4N was observed in quite significant amounts and is consumed more rapidly than formaldehyde.

As can be seen from the above survey on CO_2 laser induced ignition of condensed phase materials, most previous studies focused on ingredients of solid propellants rather than on real solid propellants. The energy fluxes of most CO_2 lasers are relatively low in comparison with those in actual rocket motors or gun chambers. The pressure range covered by the previous studies is limited to the low pressure regime [<1.379 MPa (200 psi)]. Even though these pioneering studies have contributed to the understanding of radiative ignition of condensed-phase materials, a large gap still exists in the thorough understanding of solid propellant ignition behavior under laser heating. In the past, the CO_2 laser has been used as a laboratory device for simulating convective or conductive ignition of materials used in propulsion systems. However, the actual application of the CO_2 laser as a practical ignition device could be realized in the foreseeable future. The interaction of laser beams with pyrolyzed gaseous plume would be realistic in the laser ignition process. In view of the availability of a high-powered CO_2

laser and the potential application for solid propellant ignition, laser induced pyrolysis and ignition studies of nitramine-based composite propellants have been initiated and conducted.

4.2 Method of Approach

4.2.1 Test Apparatus

A new CO_2 Laser Laboratory has been established to study the interaction of a high-powered CO_2 laser beam with various materials. Figure 25 shows the schematic diagram of the experimental setup, which includes a CO_2 laser, a beam delivery system, a test chamber, a flow visualization system, and a data acquisition system.

Figures 26a and 26b show the side and the front view of the Coherent Super 48 CO_2 laser system. This laser can be operated at a maximum power of 800 W in the continuous wave mode, and a maximum power of 3500 W in the pulsed mode. The beam delivery system includes a beam combiner for He-Ne and CO_2 lasers, a set of water-cooled mirrors, and a Kaleidoscope which is specially designed to uniformize the laser beam. The CO_2 laser beam is totally contained in the beam delivery system all the way to the test chamber. Two different test chambers, one for high-pressure ignition and the other for low pressure ignition, have been designed and fabricated. Figure 27 shows the exploded view of the high pressure windowed test chamber together with the Kaleidoscope attached to the frame close to the ceiling of the test cell.

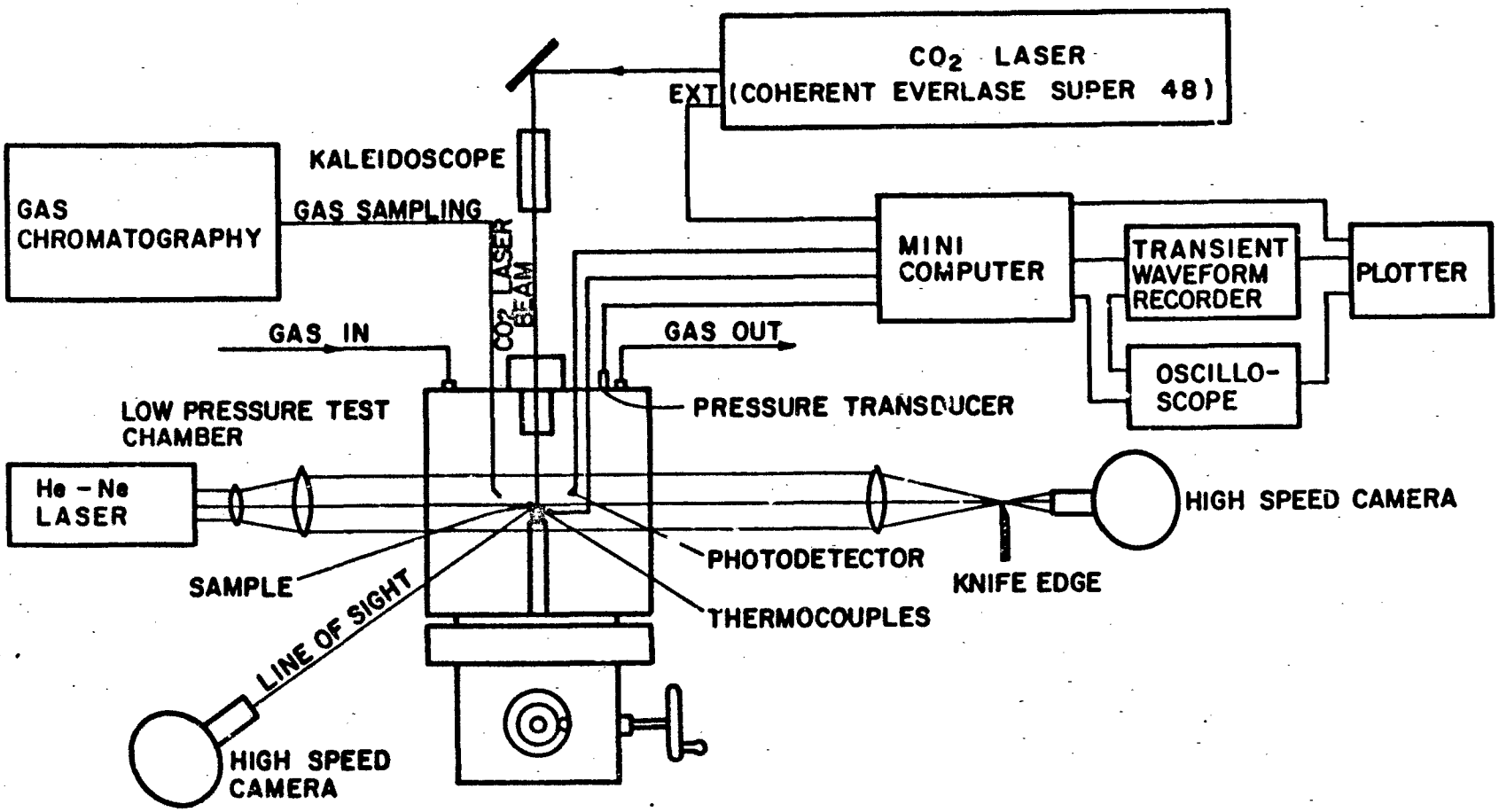

Fig. 25 Schematic Diagram of CO_2 Laser Ignition Experimental Setup

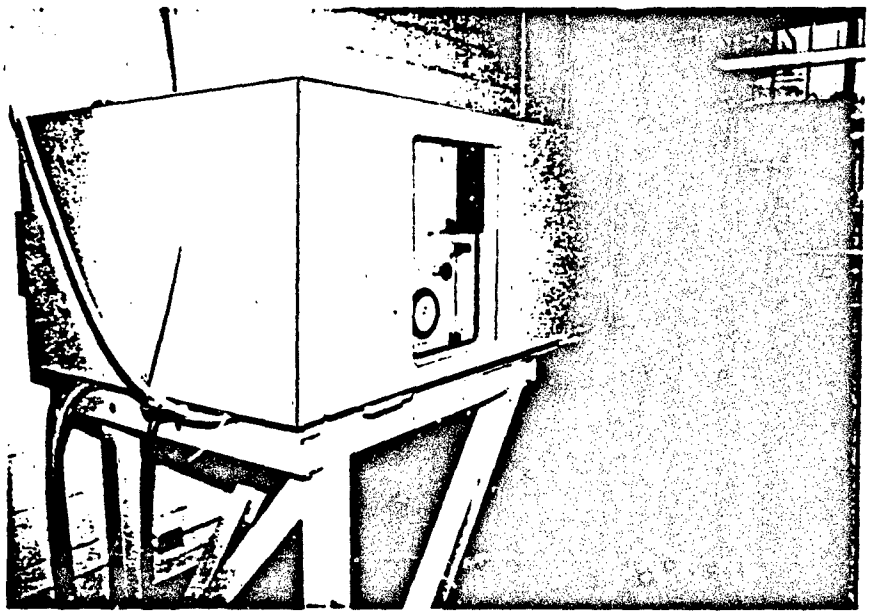

Fig. 26a Front View of CO_2 Laser System

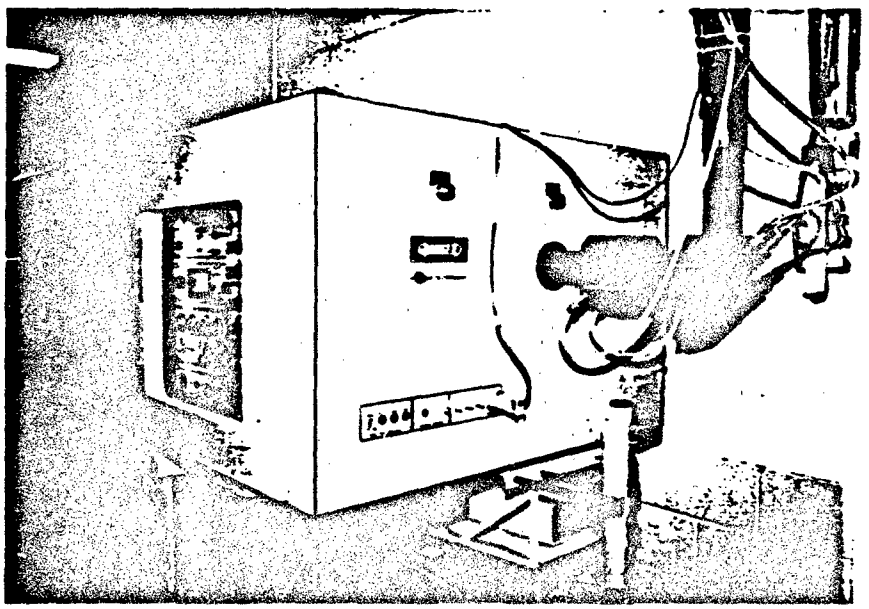

Fig. 26b Side View of CO_2 Laser System

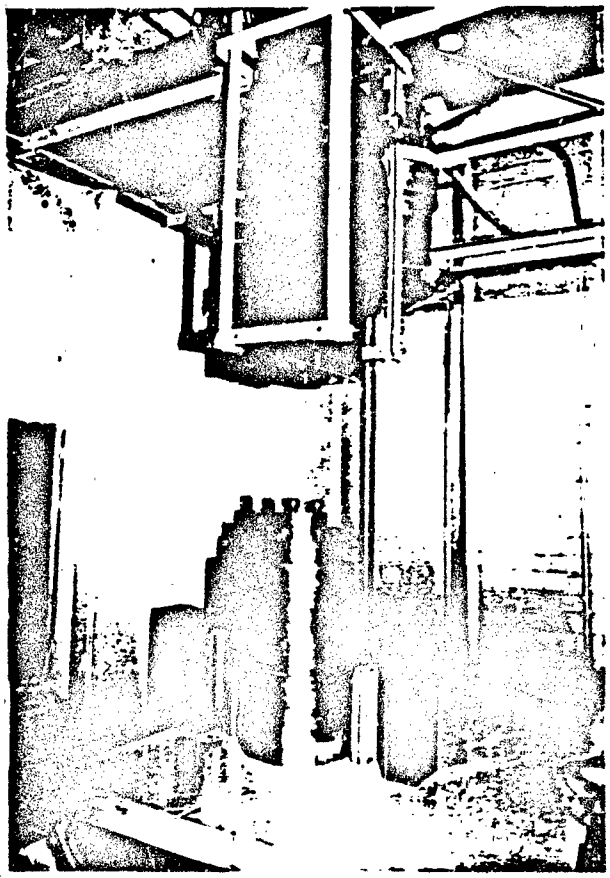

Fig. 27 CO_2 Laser Ignition Test Cell

A He-Ne laser is used for the laser schlieren photography to assist with flow visualization of the ignition events. A high-speed photographic system is used in conjunction with the schlieren system. For high pressure tests, the detailed ignition events can be observed and recorded by a separate high-speed movie camera equipped with a borescope which can provide close-up views. A Varian 3700 dual-column gas chromatograph with a Varian 4270 programmable integrator has been set up for analyzing the gaseous species pyrolyzed from the surface of test propellant samples.

Figure 28 shows the assembly drawing of the low-pressure ignition test chamber, which was designed and fabricated to ease the difficulties in flow visualization and gas sampling. The dimensions of the low-pressure chamber are 25.4 cm wide, 25.4 cm deep, and 30.48 cm high. The size of the chamber was based on various factors, such as the effects of possible disturbance by the motion of the surrounding gas, visual clearance for photography, flexibility for the installation of various probes, and handling of the samples. The four side walls of the square chamber are made of plexiglass to provide clear visual access to the sample during ignition. The top and bottom stainless steel plates are clamped together with eight steel rods. The bottom plexiglass plate is cemented to the assembly of the four side walls to eliminate sealing problems. A Ze-Se main window located at the top center of the chamber was chosen for its high transmissivity and high thermal conductivity. In order to protect the Ze-Se window from contamination by gaseous products generated from the pyrolyzed samples, a sacrificial window made of tran-

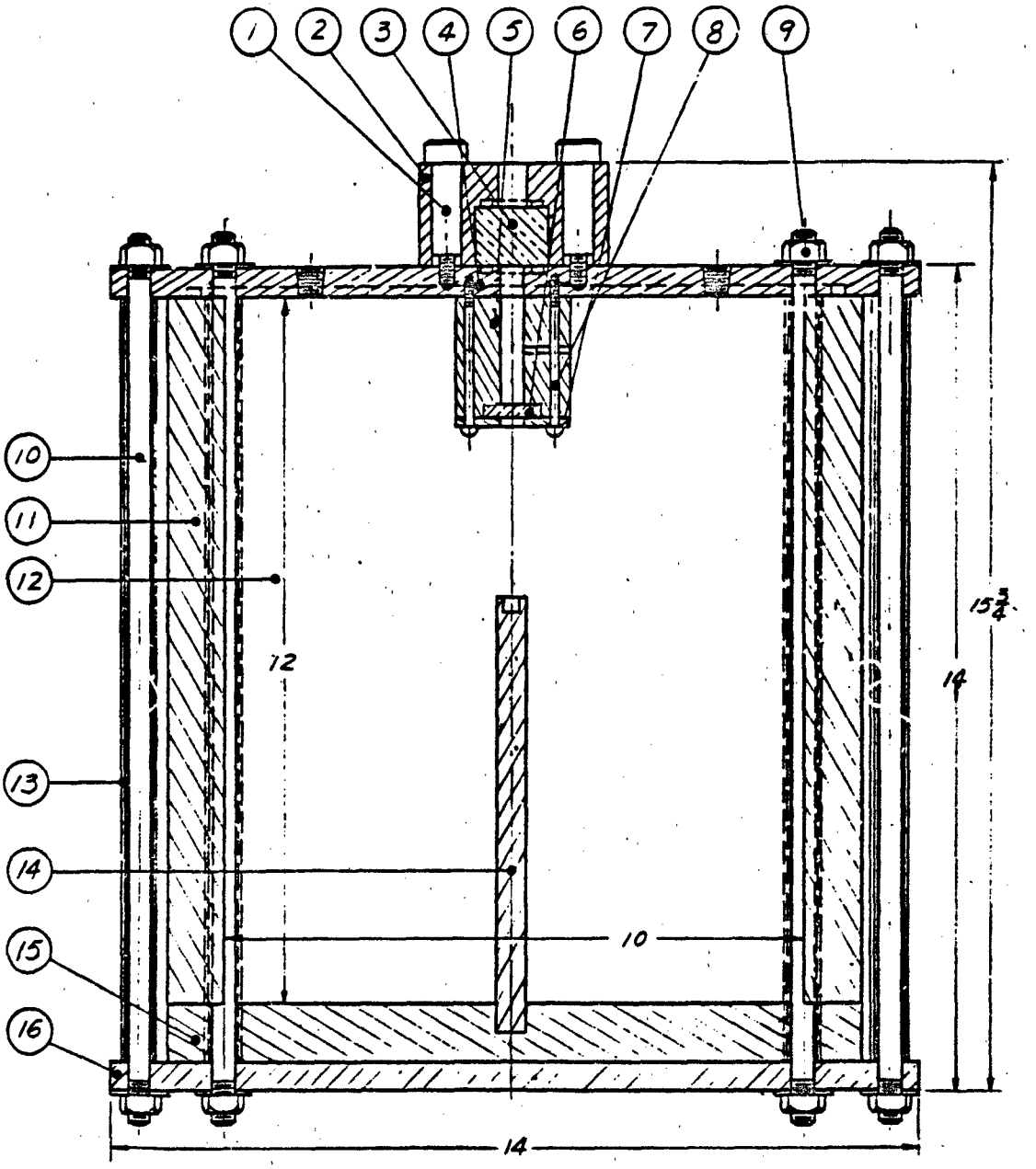

Fig. 28 Low-Pressure Ignition Test Chamber

sparent KCl material, and its holder, are installed below the main window. The KCl window was selected as the sacrificial window because it is relatively cheap and has good optical properties for CO_2 laser beam transmisson. The sample holder is a long stainless steel cylindrical rod, which can be changed readily depending upon the size of the sample and the optical arrangement of the beam delivery system.

Figure 29 shows the schematic diagram of the gas control system for the laser ignition study. Various inert gases, including He, N_2, and Ar gases, can be used as the environmental gas. Since nitrogen gas may be generated in the ignition processes, He or Ar gas is more appropriate for the ignition study of nitramine-based propellants. The gas control system is designed for both high-pressure and low-pressure test chambers. Figure 30 shows a picture of the control panel of the gas control system.

Figure 31 shows the data acqusition system which includes a mini computer system, an oscilloscope, a transient waveform recorder, and a set of charge amplifiers. The mini computer, Modular INstrument Computer (MINC), has been incoporated to control the sequences of events, to monitor the data generated, and to store and analyze the signals from various measurements. The MINC system includes a main chassis, two diskette drives, four lab modules, a monitor, a keyboard, and a printer with built-in graphic capability.

CO_2 LASER IGNITION
A SCHEMATIC DIAGRAM OF GAS CONTROL SYSTEM

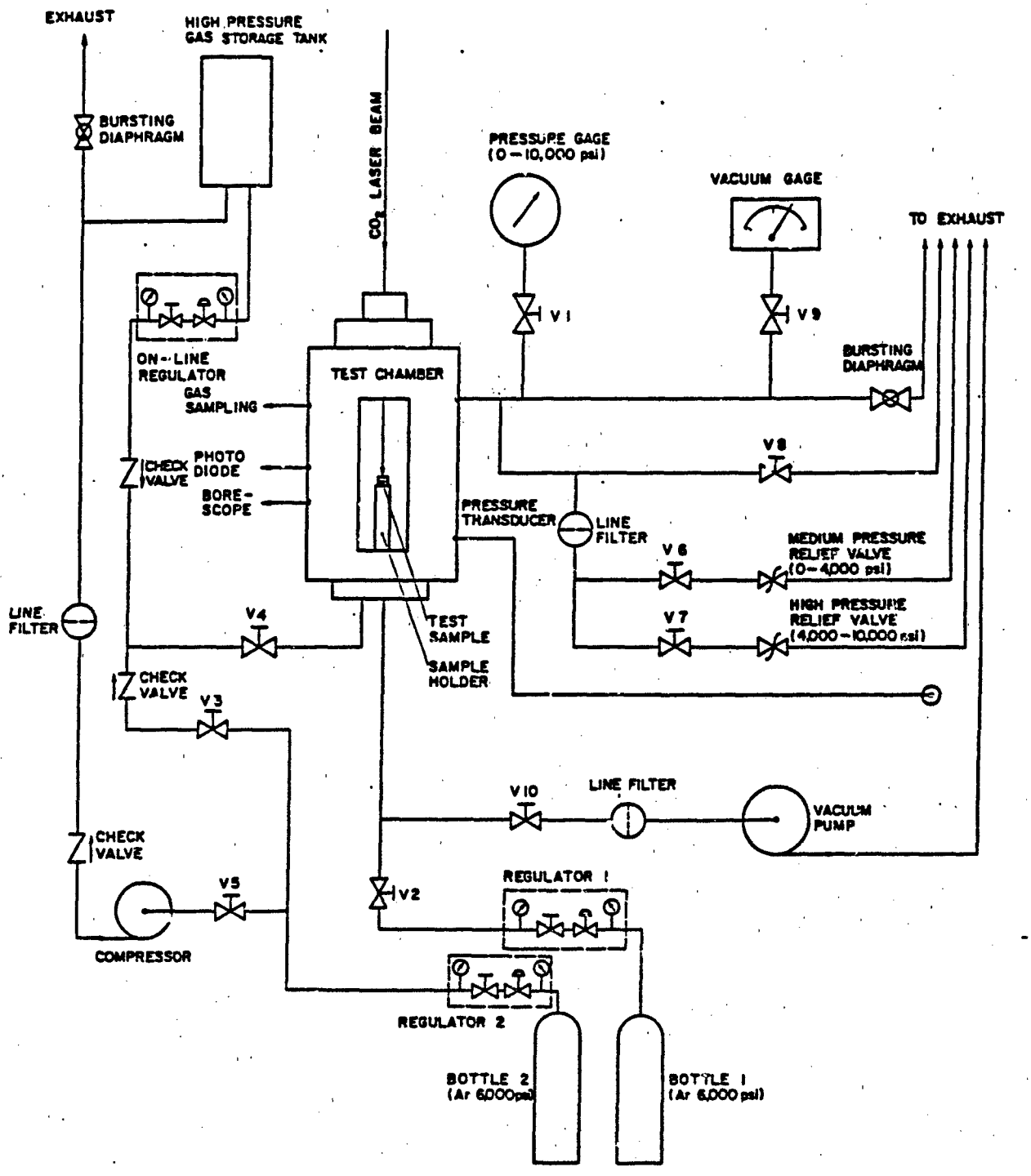

Fig. 29 Schematic Diagram of Gas Control System

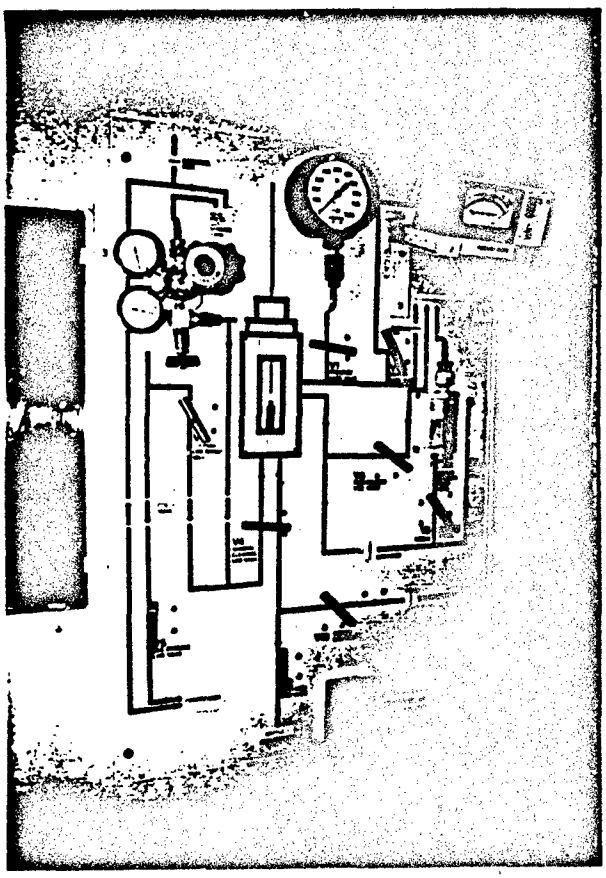

Fig. 30 Control Panel of Gas System

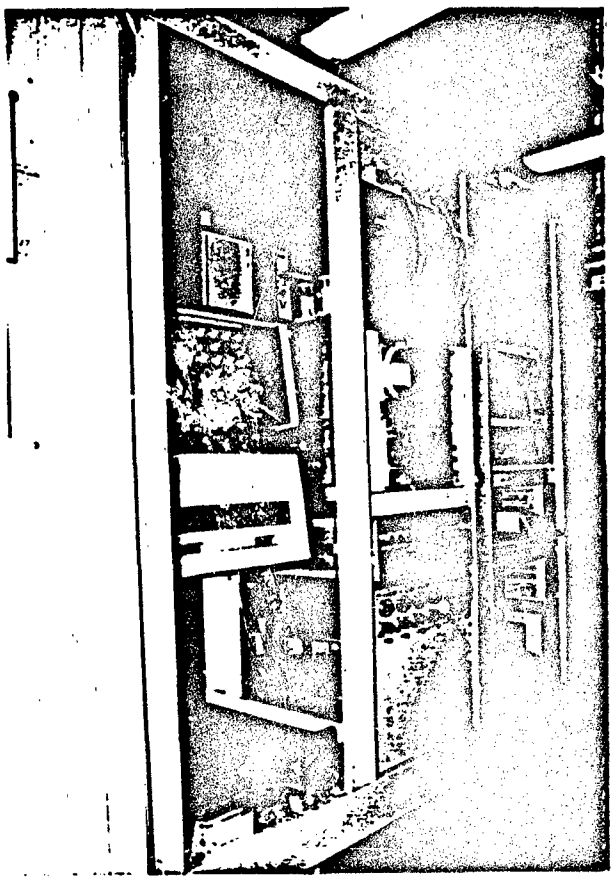

Fig. 31 Data Acquisition System

The transient waveform recorder, Biomation model 1015, is used to record transient data. The sampling rates range from 0.01 to 100,000 Hz. The memory size of the recorder is 4096 words, with 10 bits per word. An oscilloscope, Tektronix 535, is used to record two additional transient analog data. The sweep rate of the oscilloscope varies from 5 sec/cm to 1 μsec/cm. The pressure signals from transducers are amplified by a set of Dynamics charge amplifiers, model 6780. The gain range of the amplifier is 0.5 to 2500 mv/pCb, with accuracy of ±1%.

4.2.2 Safety Aspects

The laser beam is totally enclosed in the beam delivery system to reduce any possible hazards caused by emission of the laser beam. An interlocking system is in the doors of the test cell to minimize the possibility of undesirable exposure to the laser beam. The cooling water lines for each mirror, lens, and kaleidoscope are equipped with rotating indicators so that heat generated by CO_2 laser beam is removed from optical components. A safety protection system has also been designed, constructed, and installed behind the first laser mirror to detect any failure caused by overheating of the mirror system by CO_2 laser beam. Warning lights have been installed to indicate the operation of the laser system. Protective goggles that absorb near infrared radiation are worn by all test participants when the laser is in operation.

The CO_2 laser ignition work is continuing at a rapid pace. It is anticipated that useful data and observations will be obtained from this study in the near future.

REFERENCES

1. Kuo, K. K., Siefert, J. G., Mantzaras, J., Hsieh, W. H., and Koo, F., "Nitramine Propellant Crack Tip Ignition and Crack Propagation of a Burning Sample Under Rapid Pressurization," Annual Report prepared for the Office of Naval Research, Oct. 1983.

2. Kuo, K. K., Mantzaras, J., Koo, F. H., Kim, J. U., and Moreci, J., "Crack Propagation and Branching in Burning Solid Propellants and Ignition of Nitramine Based Composite Propellants Under Rapid Pressurization," Annual Report prepared for the Office of Naval Research, Dec. 1984.

3. Mantzaras, J., Andiroglu, E., and Kuo, K. K., "Recovery of Damaged Solid Propellants by Interrupting Burning and Crack Propagation Processes," 1984 JANNAF Propulsion Systems Hazards Meeting, Aberdeen Proving Ground, MD, June 18-20, 1984.

4. Kuo, K. K., Siefert, J. G., Kumar, M., Hsieh, W. H., and Andiroglu, E., "Mechanism of Crack Propagation in Burning Solid Propellants," 1983 JANNAF Propulsion Systems Hazards Meeting, CPIA Publication 381, Los Alamos, N. Mex., July 13-15, 1983, pp. 125-138.

5. Siefert, J. G. and Kuo K. K., "Crack Propagation in Burning Solid Propellants," presented at the 9th ICODERS, Poitiers, France, July 3-8, 1983. Accepted for publication in the AIAA Progress Series, Vol. 87, eds., J. R. Bowen, N. Manson, A. K. Oppenheim, and R. I. Soloukhin, 1984.

6. Kuo, K. K., Kumar, M., Wills, J. E., Siefert, J. G., Kulkarni, A. K., Andiroglu, E., Yu, S. T., and Gore, J. P., "Propellant Crack Tip Ignition and Propagation Under Rapid Pressurization," Summary Report sponsored by Office of Naval Research Power Program, Oct. 1982.

7. DeLuca, L., "Extinction Theories and Experiments," AIAA Progress Series, Vol. 90, eds., K. K. Kuo and M. Summerfield, 1984.

8. Schapery, R. A., "A Theory of Crack Initiation and Growth," International Journal of Fracture, Vol. 11, 1975, pp. 141-158, 369-387, 549-562.

9. Mueller, H. K. and Knauss, W. G., "Crack Propagation in a Linearly Viscoelastic Strip," Journal of Applied Mechanics, June 1971, pp. 141-158.

10. Dr. Kenneth K. Kuo, personal communication with R. A. Schapery, Dec. 1985

11. Erdogan, F., "Fracture Mechanics Notes," Department of Mechanical Engineering and Mechanics, Lehigh University, 1981.

12. Yu, S., Hsieh, W. H., and Kuo, K. K., "Ignition of Nitramine Propellants Under Rapid Pressurization," AIAA Paper 83-1194, 1983.

13. DeLuca, L., Caveny, L. H., Ohlemiller, T. J., and Summerfield, M., "Radiative Ignition of Double base Propellants: I. Some Formulation Effects," AIAA Journal, Vol. 14, No. 7, Jul. 1976, pp.940-946.

14. DeLuca, L., Ohlemiller, T. J., Caveny, L. H., and Summerfield, M., "Radiative Ignition of Double base Propellants: II. Pre-ignition Events and Source Effects," AIAA Journal, Vol. 14, No. 8, Aug. 1976, pp.1111-1117.

15. Birk, A., and Caveny, L. H., "Ignition of Solid Propellants Under Transient Flow Conditions," 16th JANNAF Combustion Meeting, CPIA Publ. 308, 1979, pp. 514-540.

16. Isom, K. B., Caldwell, D. J., and Greene, F. T., "Pyrolysis of Nitramine Propellants II - Kinetic Experiments," 18th JANNAF Combustion Meeting, Sept. 1980.

17. Schroeder, M. A., "Critical Analysis of Nitramine Decomposition Data: Some Comments on Chemical Mechanisms," Proceedings of the 16th JANNAF Combustion Meeting, Monterey, CA, Sept. 1979, Vol. II, pp. 13-34.

18. Schroeder, M. A., "Critical Analysis of Nitramine Decomposition Data: Activation Energies and Frequency Factors for HMX and RDX Decomposition," Proceedings of the 17th JANNAF Combustion Meeting, Hampton, VA, Sept. 1980, Vol. II, CPIA Publ. 329, pp. 493-508.

19. Schroeder, M. A., "Critical Analysis of Nitramine Decomposition Data: Product Distributions for HMX and RDX Decomposition," Proceedings of the 18th JANNAF Combustion Meeting, Pasadena, CA, Oct. 1981,CPIA Publ. 347, Vol. II, pp. 395-413.

20. Schroeder, M. A., "Critical Analysis of Nitramine Decomposition Data: Some Preliminary Comments on Autoacceleration and Autoinhibition on HMX and RDX Decomposition," Proceedings of the 19th JANNAF Combustion Meeting, Greenbelt, MD, Oct. 1982.

21. Boggs, T. L., "The Thermal Behavior of Cyclotrimethylenetrinitramine (RDX) and Cyclotetramethylenetetranitramine (HMX)," in Progress in Astronautics and Aeronautics: Fundamentals of Solid-Propellant Combustion, edited by K. K. Kuo and M. Summerfield, AIAA, 1984, Vol. 90,

pp.121-175.

22. Fifer, R. A., "Chemistry of Nitrate Ester and Nitramine Propellants," in Progress in Astronautics and Aeronautics: Fundamentals of Solid-Propellant Combustion, edited by K. K. Kuo and M. Summerfield, AIAA, 1984, Vol. 90, pp.177-237.

23. Kraeutle, K. J., "A Contribution to the Knowledge of HMX Decomposition and Application of Results," Proceedings of the 17th JANNAF Combustion Meeting, CPIA Publ. 329, Vol. II, Nov. 1980.

24. Kraeutle, K. J., "The Thermal Decomposition of HMX: Effect of Experimental Conditions and of Additives," Proceedings of the 18th JANNAF Combustion Meeting, CPIA Publ. 347, Vol. II, Oct. 1981.

25. Kraeutle, K. J., "The Differential Thermal Analysis of HMX at Atmospheric and Superatmospheric Pressures," Proceedings of the 19th JANNAF Combustion Meeting, 1982.

26. Kimura, J. and Kubota, N., "Thermal Decomposition Process of HMX," Propellants and Explosives, 5, 1980, pp. 1-8.

27. Maruizumi, H., Fukuma, D., Shirota, K., and Kubota, N., "Thermal Decomposition of RDX Composite Propellants," Propellants, Explosives, Pyrotechnics 7, pp. 40-45, 1982.

28. Kubota, N., "Combustion Mechanisms of Nitramine Composite Propellants," 18th Symposium (International) on Combustion, The Combustion Institute, 1981, pp. 187-194.

29. Kubota, N., "Physicochemical Processes of HMX Propellant Combustion," 19th Symposium (International) on Combustion, The Combustion Institute, 1982, pp. 777-785.

30. Kumar, M., Wills, J. E., Kulkarni, A. K., and Kuo, K. K., "Ignition of Composite Propellants in a Stagnation Region Under Rapid Pressure Loading," 19th Symposium (International) on Combustion, Aug. 1982, pp. 757-767.

31. Kumar, M., Wills, J. E., Kulkarni, A. K., and Kuo, K. K., "A Comprehensive Model for AP-Based Composite Propellant Ignition," AIAA Journal, Vol.22, No. 4, April 1984, pp. 526-534.

32. Private communication with E. Martin and R. Yee of U.S. Naval Weapons Center, China Lake, CA, 1984

33. Private communication with S. Mitchell of NOS and N. Gerri of Ballistic Research Lab, U.S. Army Aberdeen Proving Ground, MD, 1983

34. Fifer, R. A., "Cage Effects in the Thermal Decomposition of Nitramines and Other Energetic Materials," Proceedings of the 19th JANNAF Combustion Meeting, Oct. 6-7, 1982.

35. Karpowicz, R. J., Gelfand, L. S., and Brill, T. B., "Application of Solid-Phase Transition Kinetics to the Properties of HMX," AIAA Journal, Vol. 21, Jan. 1983, pp. 310-312.

36. Dubovitskii and Korsunskii, "Kinetics of the Thermal Decomposition of N-Nitro-Compounds," Russian Chemical Reviews, Vol. 50, No. 10, 1981, pp. 958-978.

37. McCarty, K. P., "HMX Propellant Combustion Studies: Phase I, Literature Search and Data Assessment," AFRPL-TR-76-59, Dec. 1976.

38. Shaw, R. and Walker, F. E., "Estimated Kinetics and Thermochemistry of Some Initial Unimolecular Reactions on the Thermal Decomposition of 1,3,5,7- Tetranitro- 1,3,5,7- Tetraazacyclooctane in the Gas Phase," The Journal of Physical Chemistry, Vol. 81, No. 25, 1977, pp. 2572-2576.

39. Farber, M. and Srivastava, R. D., "Mass Spectrometric Studies of the Thermal Decomposition of 1,3,5,7- Tetranitro- 1,3,5,7- Tetraazacyclooctane (HMX)," Chemical Physics Letters, Vol. 80, No. 2, June 1981, pp. 345-349.

40. Farber, M. and Srivastava, R. D., "Mass Spectrometric Investigation of The Thermal Decomposition of RDX," Chemical Physics Letter, Vol. 64, No. 2, July 1979, pp. 307-310.

41. Suryanarayana, B., Graybush, R. J., and Autera, J. R., "Thermal Degradation of Secondary Nitramines: A Nitrogen-15 Tracer Study of HMX (1,3,5,7-Tetranitro-1,3,5,7- tetraazacyclooctane)," Chemistry and Industry(London), Vol. 52, 1967, pp. 2177-2178.

42. Kim, J. U., Koo, F. H., Torikai, T., and Kuo, K. K., "Comparison of Ignition Characteristics of a Series of RDX-based Composite Propellants Under Rapid Pressurization," AIAA Paper 85-1175, presented at AIAA/SAE/ASME/ASEE 21st Joint Propulsion Conference, July, 1985 at Monterey, Ca.

43. Ohlemiller, T. J., and Summerfield, M., "Radiative Ignition of Polymeric Materials in Oxgen/Nitrogen Mixtures," Thirteenth Symposium (International) on Combustion, Combustion Institute, 1971, pp. 1087-1094.

44. Saito, T., Maruyama, T., Higashi, K., and Iwama, A., "Ignition of Laminated Composite Propellants Composed of Ammonium Perchlorate Single Crystal adn Fuel-binder Slab by Means of CO_2 Laser,"Combustion Science and Technology 15, pp. 161-168 (1977).

45. Harayama, M., Saito, T., and Iwama, A., "Ignition of Composite Solid Propellant at Subatmospheric Pressures," Combustion and Flame, Vol. 52, 1983, pp. 81-89.

46. Cook, J. R., "Laser Ignitability Applications," Internal Report of Naval Ordance Station, Indian Head, MD.

47. Kashiwagi, T., "Effects of Attenuation of Radiation on Surface Temperature for Radiative Ignition," Combustion Science and Technology, Vol. 20, 1979. pp. 225-234.

48. Kashiwagi, T., "Effects of Sample Orientation on Radiative Ignition," Combustion and Flame, Vol. 44, 1982, pp. 223-245.

49. Kashiwagi, T., "Ignition of a Liquid Fuel under High Intensity Radiation," Combustion Science and Technology, Vol. 21, 1980. pp. 131-139.

50. Kashiwagi, T., Ohlemiller, T. J., and Kashiwagi, T., "Ignition Mechanism of a Liquid Fuel by High Intensity Radiation," AIAA Paper 81-0180, 1981.

51. Mutoh, N., Hirano, T., and Akita, K., "Experimental Study of Radiative Ignition of Polymethylmethacrylate," Seventeenth Symposim (International) on Combustion, The Combustion Institue, 1978, pp. 1183-1190.

52. Beckel. S. A., and Matthews, R. D., "Ignition of Polyoxymethylene," Combustion and Flame, Vol. 57, 1984, pp. 71-86.

(DYN)

DISTRIBUTION LIST

Dr. R.S. Miller
Office of Naval Research
Code 432P
Arlington, VA 22217
(10 copies)

Dr. J. Pastine
Naval Sea Systems Command
Code 06R
Washington, DC 20362

Dr. Kenneth D. Hartman
Hercules Aerospace Division
Hercules Incorporated
Alleghany Ballistic Lab
P.O. Box 210
Washington, DC 21502

Mr. Otto K. Heiney
AFATL-DLJG
Elgin AFB, FL 32542

Dr. Merrill K. King
Atlantic Research Corp.
5390 Cherokee Avenue
Alexandria, VA 22312

Dr. R.L. Lou
Aerojet Strategic Propulsion Co.
Bldg. 05025 - Dept 5400 - MS 167
P.O. Box 15699C
Sacramenta, CA 95813

Dr. R. Olsen
Aerojet Strategic Propulsion Co.
Bldg. 05025 - Dept 5400 - MS 167
P.O. Box 15699C
Sacramento, CA 95813

Dr. Randy Peters
Aerojet Strategic Propulsion Co.
Bldg. 05025 - Dept 5400 - MS 167
P.O. Box 15699C
Sacramento, CA 95813

Dr. D. Mann
U.S. Army Research Office
Engineering Division
Box 12211
Research Triangle Park, NC 27709-2211

Dr. L.V. Schmidt
Office of Naval Technology
Code 07CT
Arlington, VA 22217

JHU Applied Physics Laboratory
ATTN: CPIA (Mr. T.W. Christian)
Johns Hopkins Rd.
Laurel, MD 20707

Dr. R. McGuire
Lawrence Livermore Laboratory
University of California
Code L-324
Livermore, CA 94550

P.A. Miller
736 Leavenworth Street, #6
San Francisco, CA 94109

Dr. W. Moniz
Naval Research Lab.
Code 6120
Washington, DC 20375

Dr. K.F. Mueller
Naval Surface Weapons Center
Code R11
White Oak
Silver Spring, MD 20910

Prof. M. Nicol
Dept. of Chemistry & Biochemistry
University of California
Los Angeles, CA 90024

Mr. L. Roslund
Naval Surface Weapons Center
Code R10C
White Oak, Silver Spring, MD 20910

Dr. David C. Sayles
Ballistic Missile Defense
Advanced Technology Center
P.O. Box 1500
Huntsville, AL 35807

(DYN)

DISTRIBUTION LIST

Mr. R. Geisler
ATTN: DY/MS-24
AFRPL
Edwards AFB, CA 93523

Naval Air Systems Command
ATTN: Mr. Bertram P. Sobers
NAVAIR-320G
Jefferson Plaza 1, RM 472
Washington, DC 20361

R.B. Steele
Aerojet Strategic Propulsion Co.
P.O. Box 15699C
Sacramento, CA 95813

Mr. M. Stosz
Naval Surface Weapons Center
Code R10B
White Oak
Silver Spring, MD 20910

Mr. E.S. Sutton
Thiokol Corporation
Elkton Division
P.O. Box 241
Elkton, MD 21921

Dr. Grant Thompson
Morton Thiokol, Inc.
Wasatch Division
MS 240 P.O. Box 524
Brigham City, UT 84302

Dr. R.S. Valentini
United Technologies Chemical Systems
P.O. Box 50015
San Jose, CA 95150-0015

Dr. R.F. Walker
Chief, Energetic Materials Division
DRSMC-LCE (D), B-3022
USA ARDC
Dover, NJ 07801

Dr. Janet Wall
Code 012
Director, Research Administration
Naval Postgraduate School
Monterey, CA 93943

Director
US Army Ballistic Research Lab.
ATTN: DRXBR-IBD
Aberdeen Proving Ground, MD 21005

Commander
US Army Missile Command
ATTN: DRSMI-RKL
Walter W. Wharton
Redstone Arsenal, AL 35898

Dr. Ingo W. May
Army Ballistic Research Lab.
ARRADCOM
Code DRXBR - 1BD
Aberdeen Proving Ground, MD 21005

Dr. E. Zimet
Office of Naval Technology
Code 071
Arlington, VA 22217

Dr. Ronald L. Derr
Naval Weapons Center
Code 389
China Lake, CA 93555

T. Boggs
Naval Weapons Center
Code 389
China Lake, CA 93555

Lee C. Estabrook, P.E.
Morton Thiokol, Inc.
P.O. Box 30058
Shreveport, Louisiana 71130

Dr. J.R. West
Morton Thiokol, Inc.
P.O. Box 30058
Shreveport, Louisiana 71130

Dr. D.D. Dillehay
Morton Thiokol, Inc.
Longhorn Division
Marshall, TX 75670

G.T. Bowman
Atlantic Research Corp.
7511 Wellington Road
Gainesville, VA 22065

(DYN)

DISTRIBUTION LIST

R.E. Shenton
Atlantic Research Corp.
7511 Wellington Road
Gainesville, VA 22065

Brian Wheatley
Atlantic Research Corp.
7511 Wellington Road
Gainesville, VA 22065

Mike Barnes
Atlantic Research Corp.
7511 Wellington Road
Gainesville, VA 22065

Mr. G. Edwards
Naval Sea Systems Command
Code 62R32
Washington, DC 20362

Dr. Lionel Dickinson
Naval Explosive Ordinance
Disposal Tech. Center
Code D
Indian Head, MD 20340

C. Dickinson
Naval Surface Weapons Center
White Oak, Code R-13
Silver Spring, MD 20910

Prof. J.T. Dickinson
Washington State University
Dept. of Physics 4
Pullman, WA 99164-2814

Prof. John Deutch
MIT
Department of Chemistry
Cambridge, MA 02139

M.H. Miles
Dept. of Physics
Washington State University
Pullman, WA 99164-2814

Dr. E.H. deButts
Hercules Aerospace Co.
P.O. Box 27408
Salt Lake City, UT 84127

Dr. T.F. Davidson
Vice President, Technical
Morton Thiokol, Inc.
Aerospace Group
110 North Wacker Drive
Chicago, Illinois 60606

David A. Flanigan
Director, Advanced Technology
Morton Thiokol, Inc.
Aerospace Group
110 North Wacker Drive
Chicago, Illinois 60606

Mr. J. Consaga
Naval Surface Weapons Center
Code R-16
Indian Head, MD 20640

Dr. L.H. Caveny
Air Force Office of Scientific
Research
Directorate of Aerospace Sciences
Bolling Air Force Base
Washington, DC 20332

Naval Sea Systems Command
ATTN: Mr. Charles M. Christensen
NAVSEA-62R2
Crystal Plaza, Bldg. 6, Rm 806
Washington, DC 20362

W.G. Roger
Code 5253
Naval Ordance Station
Indian Head, MD 20640

Mr. R. Beauregard
Naval Sea Systems Command
SEA 64E
Washington, DC 20362

Dr. Donald L. Ball
Air Force Office of Scientific
Research
Directorate of Chemical &
Atmospheric Sciences
Bolling Air Force Base
Washington, DC 20332

(DYN)

DISTRIBUTION LIST

Dr. Anthony J. Matuszko
Air Force Office of Scientific Research
Directorate of Chemical & Atmospheric Sciences
Bolling Air Force Base
Washington, DC 20332

Dr. Michael Chaykovsky
Naval Surface Weapons Center
Code R11
White Oak
Silver Spring, MD 20910

J.J. Rocchio
USA Ballistic Research Lab.
Aberdeen Proving Ground, MD 21005-5066

G.A. Zimmerman
Aerojet Tactical Systems
P.O. Box 13400
Sacramento, CA 95813

B. Swanson
INC-4 MS C-346
Los Alamos National Laboratory
Los Alamos, New Mexico 87545

Dr. James T. Bryant
Naval Weapons Center
Code 3205B
China Lake, CA 93555

Dr. L. Rothstein
Assistant Director
Naval Explosives Dev. Engineering Dept.
Naval Weapons Station
Yorktown, VA 23691

Dr. M.J. Kamlet
Naval Surface Weapons Center
Code R11
White Oak, Silver Spring, MD 20910

Dr. Henry Webster, III
Manager, Chemical Sciences Branch
ATTN: Code 5063
Crane, IN 47522

Dr. A.L. Slafkosky
Scientific Advisor
Commandant of the Marine Corps
Code RD-1
Washington, DC 20380

Dr. H.G. Adolph
Naval Surface Weapons Center
Code R11
White Oak
Silver Spring, MD 20910

U.S. Army Research Office
Chemical & Biological Sciences Division
P.O. Box 12211
Research Triangle Park, NC 27709

G. Butcher
Hercules, Inc.
MS X2H
P.O. Box 98
Magna, Utah 84044

W. Waesche
Atlantic Research Corp.
7511 Wellington Road
Gainesville, VA 22065

Dr. John S. Wilkes, Jr.
FJSRL/NC
USAF Academy, CO 80840

Dr. H. Rosenwasser
AIR-320R
Naval Air Systems Command
Washington, DC 20361

Dr. Joyce J. Kaufman
The Johns Hopkins University
Department of Chemistry
Baltimore, MD 21218

Dr. A. Nielsen
Naval Weapons Center
Code 385
China Lake, CA 93555

(DYN)

DISTRIBUTION LIST

K.D. Pae
High Pressure Materials Research Lab.
Rutgers University
P.O. Box 909
Piscataway, NJ 08854

Dr. John K. Dienes
T-3, B216
Los Alamos National Lab.
P.O. Box 1663
Los Alamos, NM 87544

A.N. Gent
Institute Polymer Science
University of Akron
Akron, OH 44325

Dr. D.A. Shockey
SRI International
333 Ravenswood Ave.
Menlo Park, CA 94025

Dr. R.B. Kruse
Morton Thiokol, Inc.
Huntsville Division
Huntsville, AL 35807-7501

G. Butcher
Hercules, Inc.
P.O. Box 98
Magna, UT 84044

W. Waesche
Atlantic Research Corp.
7511 Wellington Road
Gainesville, VA 22065

Dr. R. Bernecker
Naval Surface Weapons Center
Code R13
White Oak
Silver Spring, MD 20910

Prof. Edward Price
Georgia Institute of Tech.
School of Aerospace Engineering
Atlanta, GA 30332

J.A. Birkett
Naval Ordnance Station
Code 5253K
Indian Head, MD 20640

Prof. R.W. Armstrong
University of Maryland
Dept. of Mechanical Engineering
College Park, MD 20742

Herb Richter
Code 385
Naval Weapons Center
China Lake, CA 93555

J.T. Rosenberg
SRI International
333 Ravenswood Ave.
Menlo Park, CA 94025

G.A. Zimmerman
Aeroject Tactical Systems
P.O. Box 13400
Sacramento, CA 95813

Prof. Kenneth Kuo
Pennsylvania State University
Dept. of Mechanical Engineering
University Park, PA 16802

T.L. Boggs
Naval Weapons Center
Code 3891
China Lake, CA 93555

(DYN)

DISTRIBUTION LIST

Dr. C.S. Coffey
Naval Surface Weapons Center
Code R13
White Oak
Silver Spring, MD 20910

D. Curran
SRI International
333 Ravenswood Avenue
Menlo Park, CA 94025

E.L. Throckmorton
Code SP-2731
Strategic Systems Program Office
Crystal Mall #3, RM 1048
Washington, DC 23076

Dr. R. Martinson
Lockheed Missiles and Space Co.
Research and Development
3251 Hanover Street
Palo Alto, CA 94304

C. Gotzmer
Naval Surface Weapons Center
Code R-11
White Oak
Silver Spring, MD 20910

G.A. Lo
3251 Hanover Street
B204 Lockheed Palo Alto Research Lab
Palto Alto, CA 94304

R.A. Schapery
Civil Engineering Department
Texas A&M University
College Station, TX 77843

J.M. Culver
Strategic Systems Projects Office
SSPO/SP-2731
Crystal Mall #3, RM 1048
Washington, DC 20376

Prof. G.D. Duvall
Washington State University
Department of Physics
Pullman, WA 99163

Dr. E. Martin
Naval Weapons Center
Code 3858
China Lake, CA 93555

Dr. M. Farber
135 W. Maple Avenue
Monnovia, CA 91016

W.L. Elban
Naval Surface Weapons Center
White Oak, Bldg. 343
Silver Spring, MD 20910

G.E. Manser
Morton Thiokol
Wasatch Division
P.O. Box 524
Brigham City, UT 84302

R.G. Rosemeier
Brimrose Corporation
7720 Belair Road
Baltimore, MD 20742

Administrative Contracting
Officer (see contract for
address)
(1 copy)

Director
Naval Research Laboratory
Attn: Code 2627
Washington, DC 20375
(6 copies)

Defense Technical Information Center
Bldg. 5, Cameron Station
Alexandria, VA 22314
(12 copies)

Dr. Robert Polvani
National Bureau of Standards
Metallurgy Division
Washington, D.C. 20234

Dr. Y. Gupta
Washington State University
Department of Physics
Pullman, WA 99163